ASSESSMENT OF TIDAL STREAM ENERGY POTENTIAL FOR MARINE CORPS RECRUIT DEPOT PARRIS ISLAND

A Thesis
Presented to
The Academic Faculty

by

Thomas Gay

In Partial Fulfillment
of the Requirements for the Degree
Master of Science in the
School of Civil & Environmental Engineering

Georgia Institute of Technology
December 2010

ASSESSMENT OF TIDAL STREAM ENERGY POTENTIAL FOR MARINE CORPS RECRUIT DEPOT PARRIS ISLAND

Approved by:

Dr. Kevin Haas, Advisor
School of Civil & Environmental Engineering
Georgia Institute of Technology

Dr. Hermann Fritz
School of Civil & Environmental Engineering
Georgia Institute of Technology

Dr. Paul Work
School of Civil & Environmental Engineering
Georgia Institute of Technology

Date Approved: August 17, 2010

ACKNOWLEDGEMENTS

I would first like to acknowledge my advisor, Dr. Kevin Haas, for presenting me with the opportunity to take part in this research and for providing invaluable advice and guidance throughout the entire process. I would also like to thank Drs. Paul Work and Hermann Fritz for serving as members of my thesis committee, and for their input on all aspects of this project.

I would like to acknowledge Trent Moore and Drs. Haas and Work again for their assistance in the field work required in the execution of this study.

I would also like to thank Dr. Zafer Defne for his assistance in developing the ROMS model used in this study. That portion of the project would not have been possible without his guidance and support. Also, thanks to Dr. Lide Jiang who aided in the initial phases of the model development.

Lastly, I would like to extend my immense gratitude to my mother and father, whose continuous support has made the realization of my academic goals possible.

TABLE OF CONTENTS

LIST OF TABLES

LIST OF FIGURES

SUMMARY

The energy of the tides represents one globally existent source of renewable energy, and has the potential to play a major role in a sustainable future. An assessment of the potential for tidal energy extraction using marine current turbines at a particular location in the Beaufort River near Parris Island, South Carolina is presented in this thesis. The Marine Corps Recruit Depot located on Parris Island is situated between the confluence of the Broad and Beaufort Rivers. These rivers are tidally dominated, and experience some of the largest tidal ranges in the southeastern United States, between 2.5 and 3 meters during spring tide periods. Because Parris Island already has much of the necessary land-based infrastructure in place, there is logical potential for the extraction of kinetic energy from the nearby tidal streams using underwater turbines for power production. In order to evaluate the potential of a particular location to produce significant amounts of energy using these types of devices, extensive investigations must be conducted to determine important site characteristics such as water depth, current velocity, and water level fluctuations over time. This potential was investigated using in-situ measurements in the vicinity of the pump station on Parris Island, and by developing a numerical model of the region using the Regional Ocean Modeling System (ROMS). ROMS is a three dimensional, free-surface, terrain-following, numerical model which solves the Reynolds-averaged Navier-Stokes equations using the hydrostatic and Boussinesq approximations. The model developed for this study was calibrated using the results from the in-situ measurements, and was then used to determine the impacts of tidal energy extraction on the local flow field.

Boat-based measurements were used to determine the local bathymetry and horizontal distribution of the instantaneous currents in the vicinity of the energy plant on Parris Island. The maximum measured current speed during this portion of the study was observed near the pump house on Parris Island and was approximately 1 m/s. Longer-

term current velocity measurements were obtained for a period extending over an entire lunar month in a location determined using the results from the boat-based measurements. Measurements at this fixed location were then used to determine the tidal constituents at the site, and these in turn to predict tidal current velocities over the course of one year. Results indicate that tidal currents along the portion of the Beaufort River analyzed in this study are driven primarily by the semi-diurnal M2 tidal constituent. The tidal range at the study site is approximately 2 meters on average, and a mean depth-averaged current speed of 0.57 m/s was predicted for a time period of one year. A mean depth-averaged current velocity magnitude of 0.59 m/s was observed during the longer-term measurement period. The maximum current speed at the site is approximately 1.2 m/s near the water surface.

The ROMS model was also applied to the region, and was calibrated using the in-situ current velocity measurements. Model parameters such as bottom friction factor and wetland elevation were adjusted until current speeds and water level fluctuations predicted by the model closely resembled actual measurements. The semi-diurnal maximum currents predicted by the model are 94.5% of the actual maximum currents, on average. The average phase difference between the maximum modeled and measured tidal currents is 13.8 minutes, which is not a significant amount considering that tidal variations occur over several hours. Tidal constituents computed from the model results for current velocities and water level fluctuations also match the constituents computed from the actual measurements to a reasonable level of accuracy (i.e. within 20% for the M2, N2, K1, and S2 constituents).

The introduction of devices such as marine current turbines, which remove kinetic energy from the free stream flow, will affect both the near-field and far-field flow patterns. After calibration and validation of the ROMS model results for the undisturbed flow case, the model was then used to simulate the effects of the extraction of tidal energy on the estuarine hydrodynamics. This was done by considering four separate

extraction scenarios in which 10, 20, 30, and 60% of the total kinetic energy contained in the cross-section of the channel at the location of the ADCP deployment was dissipated by the extraction devices. The energy extraction was simulated by introducing a retarding force in the governing momentum equations in the model grid cells containing the hypothetical extraction devices. For each scenario, spatial changes in water level, current speed, and power density are examined in the vicinity of Parris Island. Water level and current speed time series from two points upstream and downstream from the extraction location, and from the extraction location itself are also examined. Results from the extraction simulations indicate that at least 370.8 MWh/month can be dissipated from the flow with minimal impacts on the local flow field. This corresponds to 61.4% of the 609.4 MWh/month of kinetic energy contained in the undisturbed flow at the extraction location.

CHAPTER 1

INTRODUCTION

The global dependence on fossil fuels as the main source of energy is becoming a major concern because of its adverse effects on the environment. In addition, these resources will soon become depleted at the current rate of exploitation (Rourke et al, 2009). To combat this dependence, research must be conducted to develop methods for utilizing various types of renewable energy that have less negative environmental impacts. The energy of the tides represents one of these types of renewable energy, and has the potential to play a major role in a sustainable future. This energy can be harnessed using extraction devices such as marine current turbines and tidal barrages. The use of turbines in tidal stream energy generation produces a significant proportion of the power that a tidal barrage scheme would generate, with far less environmental impacts (Blunden and Bahaj, 2006). The periodicity and predictability of the tides are one of the key advantages of this globally existent energy resource.

Tides are driven primarily by the gravitational forces from the Sun and the Moon acting on the Earth coupled with the Earth's rotation. Sea level rises and falls with a period of approximately 12.42 hours in most coastal locations and has a spring-neap cycle with a period of approximately 28 days. A spring tide occurs during either a full or new moon, when the gravitational forces from the Sun and Moon are both acting in the same direction. During a spring tide, the tidal range at any given location is larger than average, and thus tidal stream velocities are magnified. Conversely, during a neap tide, gravitational forces from the Sun and Moon oppose one another causing a reduction in both tidal ranges and tidal stream velocities. As the sea level rises and falls, high velocity oceanic currents develop in coastal areas which can be magnified by local topographical features such as straits, headlands, and inlets.

Since the periodicity of tides is well understood, tidal streams are predictable in phase, magnitude, and direction to a reasonable degree of accuracy for decades ahead, given accurate measurements or simulation results for a period of at least 28 days (Blunden and Bahaj, 2006). Tidal stream predictions are made by performing a tidal analysis on both the current velocity and water level time series. This type of analysis allows the time series to be decomposed into a number of harmonic constants, or tidal constituents, which describe the influence of the sun and moon on the tides at the location of the measurements. Each tidal constituent has a unique amplitude and phase at any given location. The tidal constituents and their effect on the water level at a particular location can be described by the harmonic summation

$$\eta_T(t) = \sum_{i=1}^{N} a_i \cdot \cos(\omega_i \cdot t + \varphi_i) \tag{1.1}$$

where i and N are the i^{th} constituent and total number of constituents, respectively, η_T is the water surface elevation at time t, a_i and φ_i are the amplitude and phase angle of the tidal constituent, respectively, and ω_i is the angular frequency of the tidal constituent. The objective of a tidal analysis is to determine the values of a_i and φ_i for each known ω_i. Tidal constituents of the current velocity time series can be computed using a similar approach which utilizes complex amplitudes to resolve the current direction.

There are two major types of devices currently used to extract kinetic energy from tidal streams: tidal barrages and marine current turbines. Tidal energy has been utilized on a significant scale since the construction of the La Rance tidal barrage in 1967 in France (Rourke et al., 2009). Tidal barrages use the potential energy of the tides for power generation. The basic tidal barrage setup includes embankments, sluice gates, turbines, and shipping locks. These systems can operate during either a flood or ebb tidal cycle, or both. In either case, while tidal currents are ebbing or flooding, the sluice gates are left open and a large basin is filled with water. The sluice gates are then closed during the opposite tidal cycle until a substantial hydrostatic head has developed across the barrage. At this point, the gates are opened and water flows through a system of low-

head turbines. This method of energy extraction is effective, but results in large construction costs and considerable environmental impacts.

The other major type of kinetic energy extraction device is the marine current turbine. The environmental impacts of these tidal current devices are thought to be minimal in contrast to tidal barrages (Rourke et al., 2009). Four basic types of marine current turbines exist: horizontal axis turbines, vertical axis turbines, variable foil systems, and venturi based systems which use pressure changes in flow contraction to drive secondary extraction hydraulics or pneumatics (Bryden and Couch, 2006). Horizontal and vertical axis turbines consist of a number of blades mounted on a hub, a gearbox, and a generator; flowing water drives the rotation of the rotor thus turning the generator to which the rotor is connected via the gearbox, the electricity generated can then be transmitted to land through cables (Rourke et al., 2009). Common support systems for these systems include monopoles, moored devices, floating barges, gravity based structures, and hydrodynamic down-force structures (Bryden and Melville, 2004).

The use of turbines in tidal stream energy generation produces a significant proportion of the power that a tidal barrage scheme would generate, and is less intrusive on the surrounding ecosystem (Blunden and Bahaj, 2006). Three main factors impact the effectiveness of a marine current turbine; the turbine cut-in speed (1 m/s for most turbines), the swept area of the blades, and the turbine power coefficient (Lim and Koh, 2010). It has been suggested that the horizontal option is more suitable in a marine environment as the vertical design is more susceptible to both marine growth and cavitations, reducing the efficiency of the machine (Dacre and Bullen, 2001).

The Marine Corps Recruit Depot (MCRD) located on Parris Island, South Carolina is situated at the confluence of the Broad and Beaufort Rivers (Figure 1.1). These are tidally dominated rivers, and feature among the largest tidal ranges in the southeastern United States, between 2.5 and 3 meters range at spring tide. Therefore, the

tidally driven currents (or tidal streams) in the vicinity of Parris Island potentially represent a viable, renewable resource for power generation.

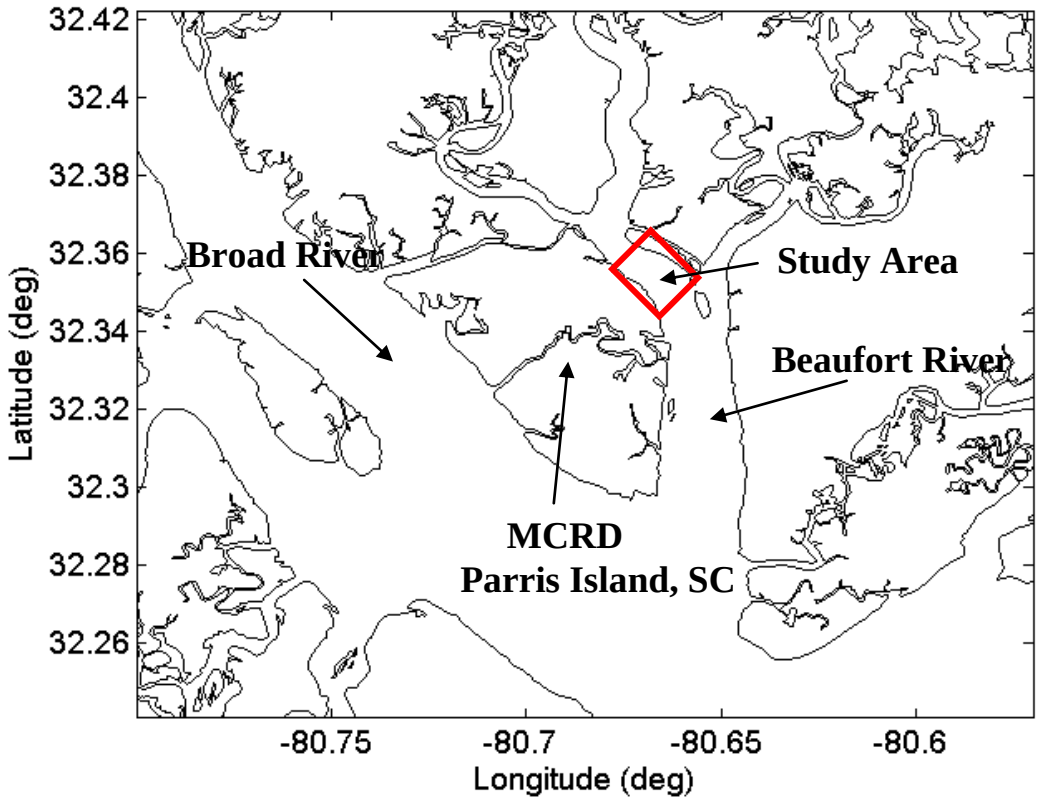

Figure 1.1. Location of Parris Island, SC relative to the Beaufort and Broad rivers, with the approximate location of the study area indicated along the Beaufort River.

In addition to the promising tidal streams, Parris Island has much of the necessary land-based infrastructure in place. Located on the eastern side of the island, shown in Figure 1.2, the Central Energy Plant (CEP) has the ability to generate 3 MW of power with steam turbines. Therefore, at least some of the infrastructure for connecting a turbine to the electrical grid is already in place. This plant is located on the shore in close proximity to the region with predicted large tidal currents. The purpose of this study is to provide an initial assessment of the actual tidal currents in order to determine the viability of energy extraction from tidal currents for Parris Island, and the impacts of doing so.

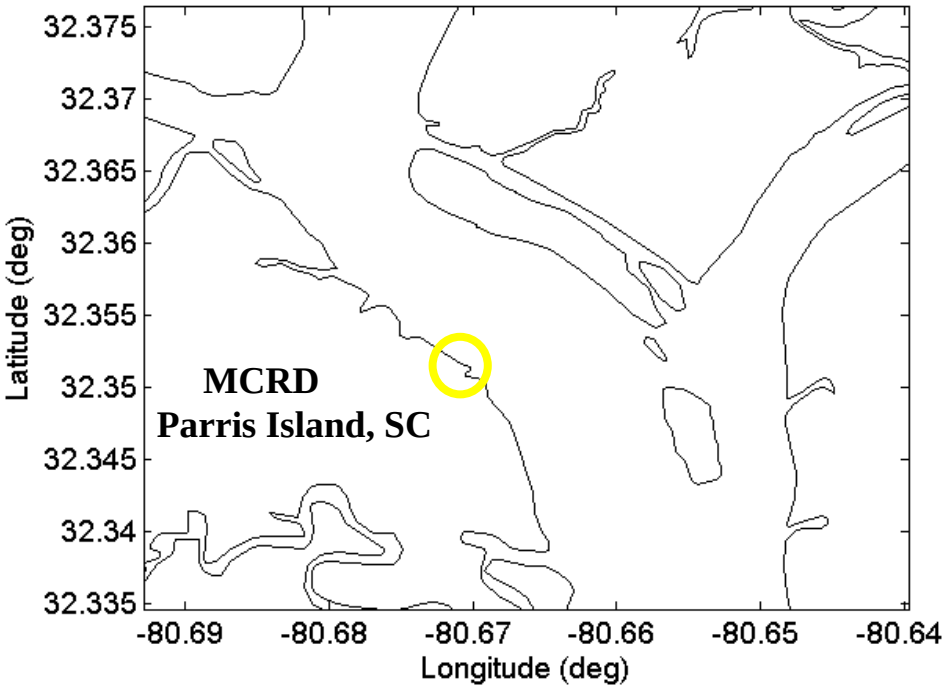

Figure 1.2. Map of the east side of Parris Island bordered by the Beaufort River. The yellow circle indicates the location of the pump station near the Central Energy Plant.

In order to accurately assess the tidal stream energy potential of the Beaufort River in the vicinity of Parris Island, a method to accurately quantify the local current velocities is required. The tidal current assessment strategy used in this study includes the following components:

1) Measurement of bathymetry for the area of interest, with survey-grade Global Positioning System (GPS) and depth sounder equipment (October 22, 2009);
2) Simultaneous measurement of velocity profiles while underway, with a down-looking acoustic Doppler current profiler (ADCP);
3) Deployment of an upward-looking ADCP on the seafloor at the location with greatest power potential, for a period exceeding a lunar month (deployed November 12, 2009, recovered December 17, 2009);
4) Application of a numerical hydrodynamic model (ROMS) to the section of coast in the vicinity of Parris Island to simulate the near-field and far-field effects of energy extraction on the estuarine hydrodynamics.

Results obtained during the initial roving survey were used to select the location at which the ADCP was deployed to collect the longer-term measurements (see Chapter 3). The ROMS model was then applied to the region and calibrated using results obtained from the longer-term deployment. The ROMS model allows for a better spatial examination of the current velocity distribution throughout the study area. These results are discussed in detail in Chapter 4. Once the model was found to have recreated the in-situ current measurements to a reasonable level of accuracy, it was used to simulate the impact of the dissipation of energy due to the placement of extraction devices near the location of the ADCP deployment. This was done by including an additional dissipation term in the governing momentum equations in the model grid cells containing the hypothetical devices. Comparisons were then made between the model results before and after the simulated placement of the turbines to develop an idea of the impact of energy extraction on the local flow field, and are presented in Chapter 5. The following chapter describes some of the major considerations in selecting a particular location for tidal energy conversion and outlines some similar tidal energy assessment studies.

CHAPTER 2

LITERATURE REVIEW

During site selection for tidal energy extraction, the characteristics of the tidal currents throughout the lunar tidal cycle must be considered in addition to the influence of energy extraction upon the underlying hydraulic nature of the tidal environment (Bryden and Couch, 2006). The assessment of the energy available in the tidal flows at a given site is an important step toward device deployment (Blunden and Bahaj, 2006). Present technology and economics dictate that only those areas where the maximum currents exceed 2 m/s are suitable for exploitation (Bryden and Melville, 2004).

Once a particular site has been proven to contain sufficient amounts of kinetic energy in its tidal streams, the appropriate turbine must then be selected. An important parameter which governs the size and number of turbines to be deployed at a chosen site is the local water depth. The turbine rotor should be placed at a location in the water column that maximizes the current speeds flowing past the blades, while remaining at a safe depth below the water surface at all times. Velocity profiles across the rotor may result in differences from expected loads and power output (Blunden and Bahaj, 2006). In some cases, restrictions in rotor diameter due to water depth may make the enhanced performance of a ducted turbine worth the extra cost involved (Blunden and Bahaj, 2006). Generally, lateral spacing between turbines is governed by installation and maintenance procedures while downstream spacing is influenced by the overall environmental impact and the effects on other devices (Shields et al., 2009).

Environmental impacts resulting from turbine placement must be considered, and are not restricted to the immediate area around the site (Bryden and Couch, 2006). Tidal power converters alter the local tidal regime, which can result in unfavorable effects on the local ecosystem (Pearce, 2005; Scott, 2007). For practical applications, the total amount of power dissipated due to the presence of extraction devices should be limited to

15-30% of the total power contained in the flow field in order to avoid any major impacts on the ecosystem (Bryden et al., 2004; Couch and Bryden, 2006; Hagerman et al., 2006c; Polagye et al., 2008). During turbine operation, water flow will be altered causing modifications to local sedimentation patterns which can lead to a change in benthic community patterns (Shields et al, 2009). Electric and magnetic fields generated by cables and energy devices may influence the behavior of some marine animals (Gill and Kimber, 2005). Furthermore, devices may act as artificial reefs which can attract different species of fish and marine mammals increasing habitat heterogeneity (Shields et al, 2009).

The severity of these environmental impacts will depend heavily on the amount of power removed from the original flow. In addition, environmental impacts will vary based on the site location and scale, the selected extraction device, the array design, the time of year, and the different phases of tidal energy development. During the construction phase, the turbines must be attached to the seafloor either directly or through the use of moorings, and cables to transmit the generated electricity must be laid in most cases (Shields et al, 2009). These processes will cause some physical disturbance of the seafloor resulting in potential habitat removal and resuspension of sediments, while noise generated during this process may lead to displacement of marine mammals, birds, and fish (Shields et al, 2009).

A large number of locations exist around the globe with promising tidal stream flow characteristics. These locations include, but are not limited to, the Arctic Ocean, the English Channel, the Gulf of Mexico, the Bay of Fundy, and the Amazon (Charlier, 2003). Although many of these areas have been recognized as potential sites for the placement of marine current turbines, few have actually been developed. Similar site assessments to that presented in this thesis have been performed in the UK (Blunden and Bahaj, 2005), Canada (Sutherland et al., 2006; Blanchfield et al., 2008), Malaysia (Lim and Koh, 2010), and the Bay of Fundy (Karsten et al, 2008). In addition, a wave and

tidal power assessment was also conducted encompassing a large portion of the southeastern United States (Defne et al., 2008; Defne et al., 2010). Three techniques are generally used to assess these locations for the extraction of tidal current energy; numerical model simulations of the currents and the effects of turbine placement, in situ current velocity measurements, and theoretical estimates of the potential power contained in the flow. When numerical modeling or theoretical estimates are used as a method for estimating tidal currents, the results are normally calibrated to agree with actual physical measurements.

Modeling the impacts of energy extraction on the flow field is an important step in obtaining preliminary estimates of the overall effects on the local ecosystem. Since these effects can potentially be observed several kilometers from the extraction location, it is necessary to model the tidal currents at an estuary scale (Defne et al., 2010). Examples of some two dimensional numerical models that can be used to model tidal currents include MIKE21(DHI, 2008), TELEMAC (TELEMAC, 2008), DIVAST (CU, 2008), and TIDE2D (Sutherland et al., 2007; Triton Consultants Ltd., 2002), among others. However, these models are not suitable to model flow around the energy extraction devices and it is numerically too expensive to model at an estuary scale using three-dimensional full Navier-Stokes solvers (Defne et al., 2010). Therefore, a momentum sink is generally introduced into the governing momentum equations to simulate the energy extraction process (Bryden and Melville, 2004; Garrett and Cummins, 2004; Bryden and Couch, 2006).

Tidal stream energy resources at Portland Bill, UK were evaluated using a two-dimensional tidally driven hydrodynamic numerical model developed using the TELEMAC system (Blunden and Bahaj, 2005). This site experiences complex flow patterns around a headland where large eddies and breaking waves occur frequently. The model results were used to produce a tidal stream velocity time series over the simulation period with observed current speeds up to 3.6 m/s. Validation of the model was done

using actual tidal elevation measurements. Another similar study in the UK was performed in the Pentland Firth, Scotland, with emphasis on the ecological impacts of turbine placement (Shields et al, 2009). For this region, it is strongly recommended that baseline surveys of intertidal and sub tidal regions, assessments of the importance of the area for fish stocks, birds, and marine mammals, and investigations on how device design might influence surrounding marine biota and their communities be taken into account (Shields et al, 2009). In the Pentland Firth, maximum tidal stream velocities of 5.7 m/s were observed with a mean spring velocity of 2.9 m/s in the most energetic region.

A tidal current energy assessment was completed in Johnstone Strait near Vancouver Island, Canada (Sutherland et al, 2006). In this study, the tidal power potential of the area was simulated using a two-dimensional finite element numerical model, TIDE2D. The placement of turbines was simulated by increasing the drag in the areas with favorable conditions for energy extraction. In Johnstone Strait, the maximum extractable energy was found to be 1335 MW and current speeds reach a maximum value of 7.7 m/s in Seymour Narrows. The model considers only the M2 tidal constituent in order to reduce computation time. Bottom friction was higher in the model than in actuality to account for additional dissipation mechanisms that are not accounted for by the model. This value was chosen so that the modeled tidal elevations match actual observations.

In Malaysia, tidal energy is being considered due to the rapidly diminishing fossil fuel reserves and the negative environmental impacts associated with the use of those energy sources (Lim and Koh, 2010). A three-dimensional numerical model developed using the Princeton Ocean Model (Mellor, 2003) was used to assess the amount of energy that could potentially be generated by marine current turbines in the area. Economic viability and environmental impacts were also considered. The model was calibrated against actual measurements using an adjoint data assimilation approach. Actual measurements were obtained from tidal observations records and a global tidal property

database (TPXO) (Egbert et al., 1994). It was concluded that a combined total of about 14.5 GWh of electricity could be generated per year in the most energetic regions off the coast of Malaysia. At this rate, it was estimated to take approximately 10 years for owners of the installed marine current turbines at this location to recover their economic investments.

The Bay of Fundy experiences one of the largest tidal ranges in the world at about 6 meters amplitude in the Minas Basin. The tidal power available in the Minas Passage in the Bay of Fundy was considered for electricity generation using in-stream turbines (Karsten et al, 2008). A theoretical model developed by Garrett and Cummins (2005) was used to calculate the potential power generated from the tidal flows in the channel. The model also considers the effect of turbine drag on both the flow and the tidal amplitude. The volumetric flow rate through the passage was found to be roughly 10^6 m^3/s, and the time and depth-averaged currents are estimated at 3.28 m/s. The tides were simulated using a two-dimensional, finite-volume model (FVCOM) (Chen et al., 2006) and were used to verify the theoretical estimates and to examine the far-field effects of power extraction. It was determined that a maximum of 7 GW of power could be extracted from the Minas Passage. However, extracting the maximum amount of power would result in a reduction in the tides in the Minas Passage and the Minas Basin of 36%, leading to an increase in the tides in the Bay of Fundy—Gulf of Maine system of 15%. In this case, extracting power actually increases the tidal head across the channel and the forcing that drives the flow.

An assessment of the wave and tidal power potential was conducted in the coastal regions of North Carolina, South Carolina, Georgia, and northern Florida (Defne et al., 2008; Defne et al., 2010). The tidal stream power was evaluated only along the coast of Georgia with the ROMS model, similar to that utilized in this study, and validated using actual measurements. Results from the model suggest that this region has low to moderate (< 0.8 m/s) tidal currents along most of the coast, on average. Part of the

Intracoastal Waterway between the Altamaha and Doboy Sounds and a part of the Canoochee River were found to have the highest tidal power densities on the Georgia coast. Using one-month model simulations, the tidal power densities at these locations were computed to be about 1600 W/m^2, 1400 W/m^2, and 1100 W/m^2, respectively. The effect of energy extraction on the estuarine hydrodynamics was also simulated using an additional retarding force in the governing momentum equations in the ROMS model.

Although many locations with significant tidal current energy exist globally, tidal current turbine technology is currently not considered to be economically viable on a large scale, as it is still in the early stages of development (Rourke et al, 2009). Current issues restricting development are installation challenges, maintenance, electricity transmission, loading conditions, and environmental impacts (Rourke et al, 2009). Effective device mounting represents a particularly significant cost challenge, whether on the seafloor or near the water surface (Bryden and Couch, 2006). The environmental impacts of power extraction using marine current turbines are still a popular research topic, as little is understood concerning those issues. Economically, only those locations that experience tidal current velocities over 2 m/s could feasibly be developed. As technology advances, however, energy extraction may become possible at lower current speeds. Much more research and development is necessary if tidal energy extraction is to be implemented on a significant scale.

CHAPTER 3

TIDAL CURRENT AND DEPTH MEASUREMENTS

In order to assess the potential for the conversion of tidal current energy at Parris Island, current velocity and bathymetric profiles were established in order to determine the most energetic portion of the area of interest. Once this was established, a more detailed investigation of important characteristics such as current velocity and water level fluctuations over the course of an entire lunar month was performed at this location. The most direct method used to obtain this information is to implement in-situ measurement techniques. In-situ data can not only be used to gain an initial idea of the tidal stream energy potential at a site, but can also be used in the calibration and validation of other assessment methods such as numerical hydrodynamic modeling.

The bathymetric survey and boat-based current velocity measurements took place over the course of one day near the pump house on the northeastern side of Parris Island. A survey-grade Global Positioning System (GPS), fathometers, and an acoustic Doppler current profiler (ADCP) were used aboard a 7 m vessel. After post-processing of the roving survey data, the bathymetry and current velocity datasets were established, and the area where the strongest tidal currents occur was determined. A standalone ADCP was deployed on the riverbed at this location for a period exceeding one lunar month.

An ADCP is an acoustic instrument which uses the Doppler effect to determine the speed and direction of the flowing water. The instrument used in this study sends pulses of sound through the water column in four different known directions. As the sound is reflected back to the instrument off of particles suspended in the water column, it changes frequencies due to the movement of the water. The computed change in frequency, arising from the Doppler effect, is then used to calculate the velocity of the water throughout the water column. The ADCP reports three components of velocity as a

function of distance from the instrument, at a nominal rate of 1 Hz. This data is then averaged to remove some of the noise inherent in the single-ping data. Since every measurement occurs at a slightly different time and location when deployed from a moving vessel, the resulting dataset is not an instantaneous snapshot of the velocity field, but can effectively show how velocities vary at a site. The ADCP used in this study is shown in Figure 3.1.

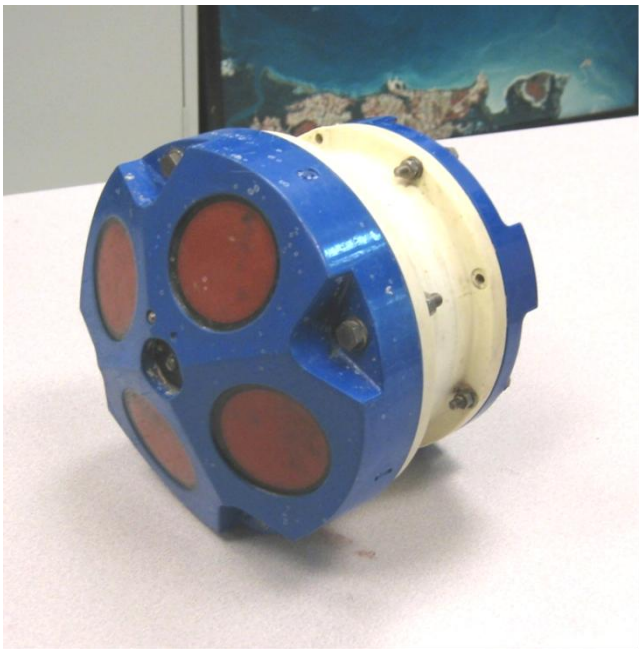

Figure 3.1. Teledyne RD Instruments ADCP used in this study.

The ADCP can be used either in upward or downward-looking mode. When the device is deployed at a fixed point on the seafloor, upward-looking mode is used, whereas downward-looking mode is often used when deployed from a moving vessel. It is necessary to also know the velocity vector for the boat when the ADCP is deployed in downward-looking mode. This can either be determined using GPS data or a bottom-tracking algorithm built into the ADCP. In this study, the latter option was used.

A fathometer is also an acoustic device, but the signal processing is much simpler. Fathometers measure depth at a point, therefore, the quantity of interest is the travel time

for each pulse of sound to travel to the seafloor and back. With this information, the distance from the acoustic transducer to the seafloor can be computed. The speed of sound in water, which is a function of the water temperature and salinity, must be known for this computation.

3.1 Boat-based Measurement Methodology

The one-day roving survey occurred on Thursday, October 22, 2009. Prior to arrival at the site, a surveying strategy was defined including multiple tracks nominally normal to the river bank, approximately 250 m apart, and extending across the river to the Intracoastal Waterway, which parallels the bank at the site. Multiple boat runs in a "zig-zag" pattern were completed along the bank of the Parris Island side of the river to produce more detailed observations of currents and bathymetry, due to the logistical advantages of placing turbines close to the energy plant. Additional survey lines were planned along the river's axis. Drs. Paul Work and Kevin Haas, and Thomas Gay (all from Georgia Tech Savannah) took part in the roving survey.

A dual-frequency digital fathometer system (Bruttour Ceeducer) was deployed through the "moon pool" toward the bow of the vessel, and can be seen in Figure 3.2. Prior to the survey, field calibration of the depth sounders was completed. A large aluminum plate was lowered into the water column beneath the instruments at several known depths and the measurements were checked for accuracy. The transducers used were 200 and 30 kHz, respectively. Since lower frequency signals tend to penetrate deeper into the bed, it is sometimes possible to identify locations of soft mud banks when two frequencies are used. For the completed survey in this study, output from the two matched closely, and it was established later that the site of greatest interest features a firm shell hash layer over consolidated mud.

Figure 3.2. Transducers measuring depth deployed through "moon pool" on survey boat. 200 kHz transducer to left (toward bow) and 30 kHz transducer to right in photo.

Ashtech Z-12 and Z-Surveyor dual-frequency receivers were used to acquire x-y-z positioning data for the survey vessel. A base station was set up on land near the energy plant at Parris Island. This station, logging data at a known, fixed point, allowed determination of time-dependent position errors that were used to correct the data from the roving receiver. Data was collected at 5 Hz on the boat as it traversed the site, and was post-processed using GrafNav software to apply kinematic corrections. The GPS and fathometer data were used in combination to measure the elevation of the seafloor, and a datum conversion was applied so that depth measurements became relative to the Mean Lower Low Water (MLLW) level. While the fathometer measured the depth to the seafloor, the GPS receiver simultaneously reported antenna height. The elevation of the seafloor was then computed as follows

$$z_{seafloor} = z_{ant} - h_{ant} - DB_t \tag{3.1}$$

where z_{ant} is the height of the GPS antenna as recorded by the GPS, h_{ant} is the fixed vertical distance from the fathometer transducer to the GPS antenna, DB_t is the depth of the seafloor as measured by the fathometer, and $z_{seafloor}$is the elevation of the seafloor.

A 1200 kHz RD Instruments ADCP equipped with a bottom tracking option was mounted off the bow of the survey boat (Figure 3.3). Together with the fathometer system, these instruments allowed simultaneous measurements of water depth and water velocity profile beneath the boat, with each parameter typically measured at least once per second. These measurements were coupled with the GPS data to continuously track the measurement locations. Data was logged using Hypack surveying software.

Figure 3.3. 1200 kHz RD Instruments ADCP deployed off bow of survey vessel.

3.2 In-situ Measurement Methodology

The same ADCP used for the small vessel-based measurements described above was mounted in a T-shaped frame for longer-term deployment on the riverbed (Figure 3.4). The instrument was deployed in standalone mode with two battery packs from Thursday, November 12, 2009 to Thursday, December 17, 2009. It was programmed to record a three-minute average velocity profile every fifteen minutes, with 0.5 m vertical resolution. This data was averaged internally to yield one estimate of the velocity profile every fifteen minutes, averaged over each three-minute measurement period.

Figure 3.4. 1200 kHz ADCP mounted in aluminum frame for deployment on river bed, November 12, 2009.

The instrument was lowered to the seafloor and secured by divers with anchors on each end. A line was run to shore for later recovery. Dr. Paul Work (Georgia Tech Savannah), Trent Moore (Skidaway Institute of Oceanography), and Thomas Gay (Georgia Tech Savannah) were involved in the instrument deployment, which occurred near slack low tide. The ADCP deployment location coordinates (shown in Figure 3.5) are: 32° 21.191' N, 80° 40.228' W. Prior to deployment, the riverbed at the site was found to be oyster shell hash over consolidated mud.

A return trip to Parris Island to recover the standalone ADCP occurred on December 17, 2009. Previously, a Sonotronics "pinger" was installed on the instrument frame to be used if the land line to the instrument had been damaged. An underwater listening device can be used to locate the instrument this way, but was not needed on this site visit. The instrument was recovered using the land line attached to the frame during deployment. The instrument was still pinging when unplugged from its power source at roughly 22:00 GMT on December 17, 2009. The data was downloaded to reveal that the

instrument had been recording as planned for the entire deployment period. Drs. Paul Work and Kevin Haas (Georgia Tech Savannah), Trent Moore (Skidaway Institute of Oceanography), and Thomas Gay (Georgia Tech Savannah) were present during the instrument recovery.

Measurements from the standalone ADCP deployment were used to determine the tidal constituents of both the water level and currents. These constituents may be used to produce predictions of tidal stage time series for any subsequent period of time. The data was then used to compute velocity and power density probability histograms at the chosen location, which will be presented in the next section.

3.3 Results

Results from all three datasets (bathymetric survey, roving ADCP, and fixed ADCP) are presented below.

3.3.1 Boat-based Measurements

Current velocity and depth data collected during the boat-based survey was synchronized with the position data obtained from the GPS using the time stamp from each measurement. Figure 3.5 shows the bathymetry measurements taken throughout the day on Thursday, October 22, 2009. In the figure, blue coloration represents larger water depths while red coloration represents shallower depths. Water depths are relative to the mean lower low water level (MLLW). The deepest measured portion of the river is located along the bank near the pump station on Parris Island. Water depths are shallower on the northeast side of the river on the side of the Intracoastal Waterway opposite from the area of interest. In each of the next three figures, the location of the longer-term ADCP deployment is indicated with an "x" (Northing: 3579632 m, Easting: 531006 m).

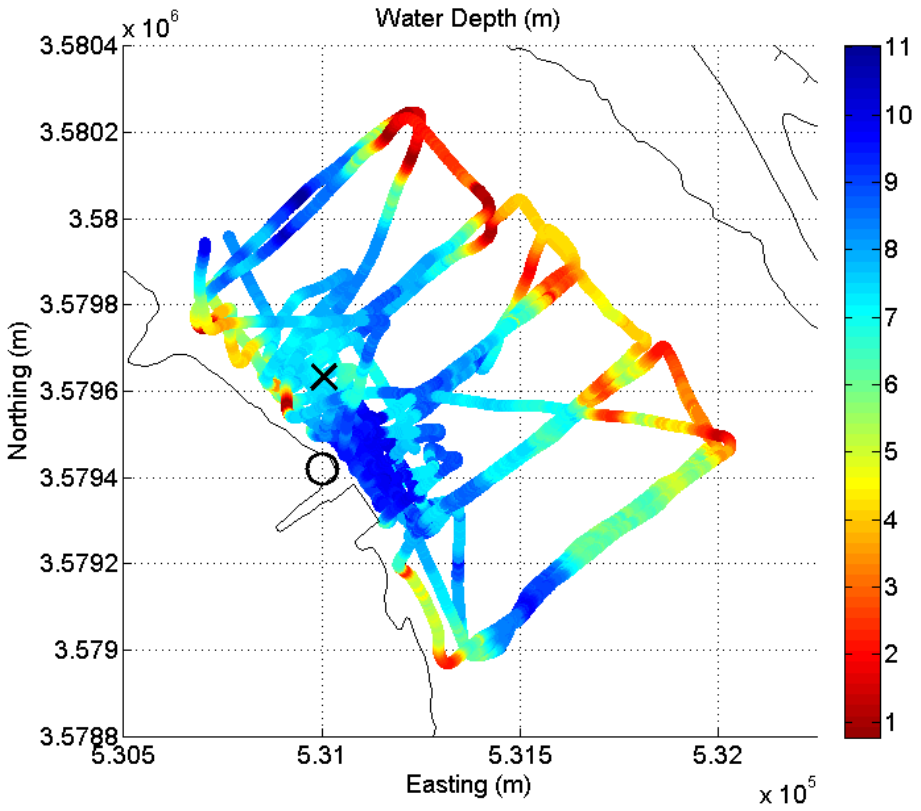

Figure 3.5. Bathymetry (relative to MLLW) of the study area with the location of the longer-term ADCP deployment denoted by an "x" and the location of the pump station indicated by the circle. Blue indicates deeper water and red indicates shallower water.

During the morning of October 22, 2009, current measurements were taken simultaneously with bathymetry measurements during the flood tidal cycle. Depth-averaged current velocity measurements taken during the flood portion of the tidal cycle are presented in Figure 3.6. In the figure, the highest current speeds are shown in red while the smallest speeds are shown in blue. The maximum current speed during the flood tidal cycle at the site was approximately 0.9 m/s on the date of measurement. The ADCP used in this study measures current speeds with an estimated accuracy of +/- 6 cm/s for the roving measurements (Teledyne RD Instruments, 2008).

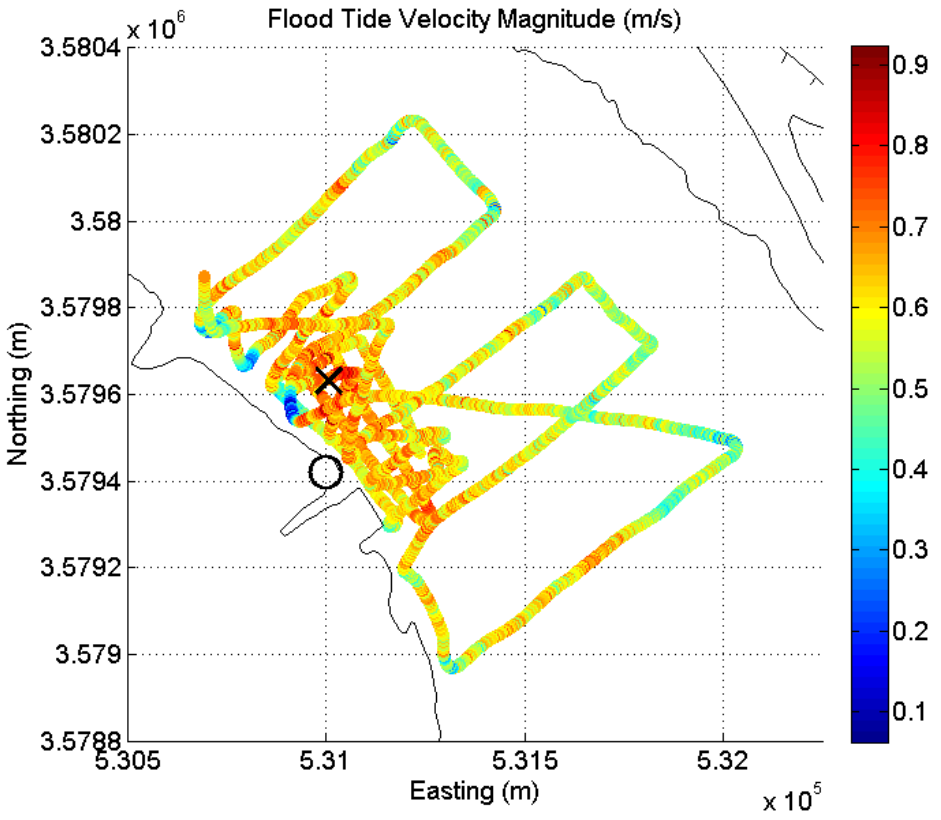

Figure 3.6. Depth-averaged current velocity magnitude measured during the flood tidal cycle on October 22, 2009, with the location of the long-term ADCP deployment denoted by an "x" and the location of the pump station indicated by the circle. Red indicates faster current speed and blue indicates slower current speed.

Current and bathymetry measurements were also taken during the ebb tidal cycle in the afternoon of October 22, 2009. Figure 3.7, below, is a plot similar to Figure 3.6. During the ebb tidal cycle, maximum depth-averaged current velocities are slightly higher at approximately 1.1 m/s. The location of maximum current velocity during the ebb portion of the cycle was similar to that found during the flood tidal cycle. The location of the standalone ADCP was chosen based on the location of the maximum measured currents, which were found near the following location: 32° 21.184' N, 80° 40.223' W.

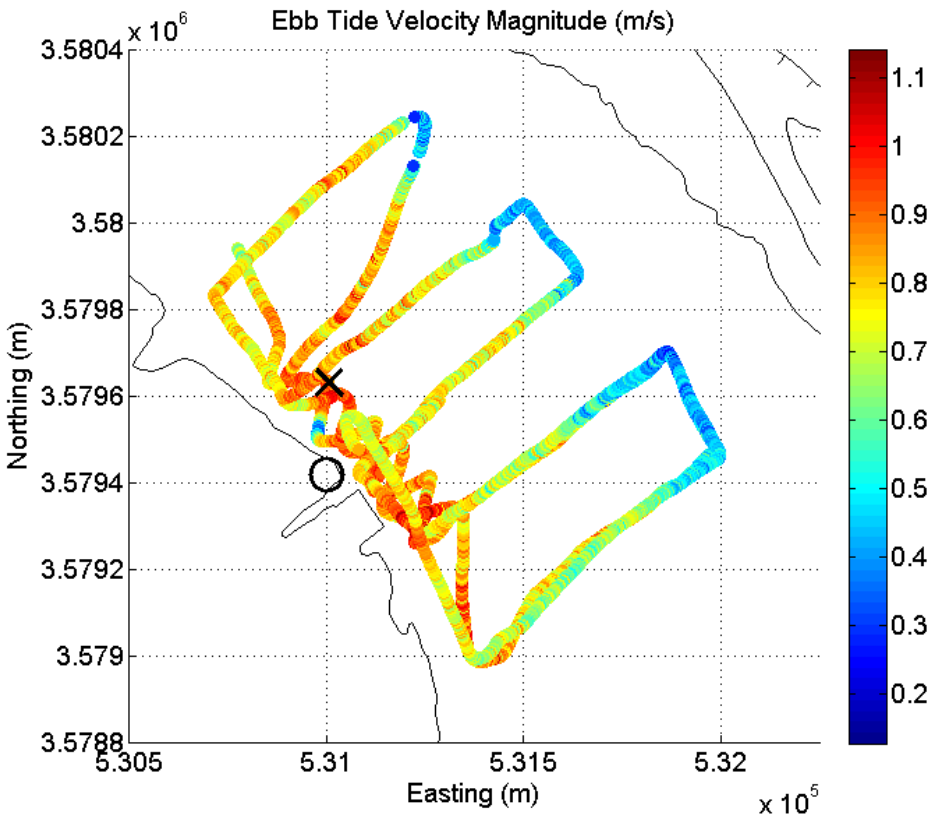

Figure 3.7. Depth averaged current velocity magnitude measured during the ebb tidal cycle on October 22, 2009, with the location of the long-term ADCP deployment denoted by an "x" and the location of the pump station indicated by the circle. Red indicates faster current speed and blue indicates slower current speed.

3.3.2 In-situ Measurements

The standalone ADCP was deployed over 35 days from Thursday, November 12 to Thursday, December 17, 2009. Three vertical profiles of the velocity magnitude are plotted over depth up to the mean water level (MWL) from this measurement period and are displayed in Figure 3.8. Time-averaged current magnitudes from one of the strongest ebb tidal cycles, which occurred on December 3, 2009, are denoted by the blue line in the figure. The mean current, averaged over the three-hour portion of the ebb tidal cycle in which the currents were strongest, reaches a maximum-of approximately 0.96 m/s at the water surface. The red line is a similar profile, but displays current velocity magnitudes

from one of the strongest flood tidal cycles, occurring on December 2, 2009. This profile is averaged over the three-hour portion of the flood tidal cycle in which the currents were strongest. Note that the maximum mean current velocity (0.87 m/s) is still found at the water surface, but is slightly lower than that of the ebb portion of the tidal cycle. In each profile, current velocity is at a maximum at the water surface and decreases with depth into the water column due to bottom friction and viscous effects. The peak, averaged current velocity magnitude over the entire measurement period occurred at the water surface, and was calculated to be approximately 0.66 m/s.

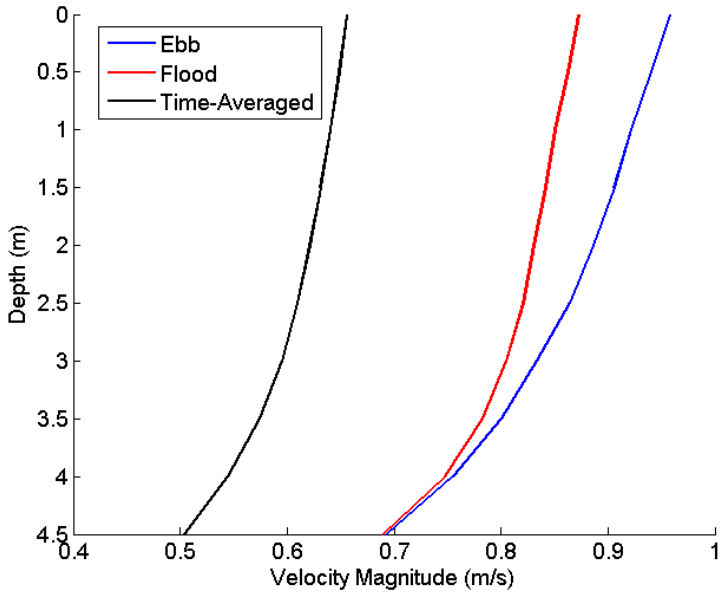

Figure 3.8. Vertical current speed profiles at the location of the fixed ADCP, averaged over one ebb tidal phase on December 3, 2009, one flood tidal phase on December 2, 2009, and the entire measurement period.

Once data from the long-term ADCP deployment had been recovered, the measured data was investigated via harmonic analysis using the Matlab toolbox, "T-Tide" (Pawlowicz et al, 2002). Because tidal flows are driven by the Sun and Moon, and the locations of the Sun and Moon are well predicted from astronomy based on orbits with various known periods, the water level and currents may be decomposed to tidal

constituents consisting of amplitudes and phases for the known components. Each constituent represents the gravitational force between the Earth and another celestial body (the Moon, the Sun, etc.) which produces an independent, periodic tidal change. With the constituents known, predicted tides can then be computed. In order to perform meaningful decomposition, a time series of at least one lunar month (29-1/2 days) must be collected. In this study, data was collected for a period exceeding one lunar month, and the results of the tidal decomposition are shown below in Table 3.1 and the figures that follow. The site is dominated by the M2 tidal constituent, which is semi-diurnal and is caused by the gravitational force of the moon.

Table 3.1. Significant depth-averaged tidal constituents and their properties derived from fixed ADCP velocity and stage measurements. Velocity inclination corresponds to compass heading of major axis of tidal ellipse, the inclination of the shoreline is 122 degrees at the measurement location.

Constituent	**Frequency**	**Water Level Amplitude**	**Water Level Phase**	**Velocity Amplitude**	**Velocity Phase**	**Velocity Inclination**
	hr^{-1}	**m**	**degrees**	**m/s**	**degrees**	**degrees**
M2	0.0805	0.86	31.0	0.87	318	120
N2	0.0790	0.19	26.4	0.18	311	119
K1	0.0418	0.12	205	0.070	120	119
S2	0.0833	0.11	52.5	0.11	348	121
MM	0.0015	0.11	148	0.010	218	51.9
O1	0.0387	0.062	218	0.038	123	119
L2	0.0820	0.054	46.9	0.080	327	120
M4	0.1610	0.053	246	0.062	88.7	115
M6	0.2415	0.026	136	0.062	74.3	122

Current velocity and water level predictions computed from the constituents were compared to the actual measured values over the ADCP deployment time period. This comparison is necessary to check that the majority of the flow is captured by the

calculated tidal constituents. Actual field measurements of current velocity include effects from freshwater inputs, wind-driven flows, and tidal flows. The predictions made through the tidal decomposition only include effects of tidally driven flows, and will differ somewhat from measured current velocities and water levels. Once the results from the tidal decomposition are validated by actual measurements, future predictions can be made with greater confidence.

The predicted and measured fluctuations in water level at the instrument location are compared in Figure 3.9. The average mean water level (MWL) over the entire measurement time period was calculated to be 5.1 meters relative to the riverbed. The measured water depth ranged from a minimum of 3.8 meters to a maximum of 6.7 meters. Again, the predictions obtained from the tidal decomposition match the actual measurements very well. The two data sets are in phase throughout the measurement time period, and only minor differences occur at the maximum and minimum depth values. The average magnitude of the difference between the measured and predicted water level values over the entire measurement period is 0.1 m.

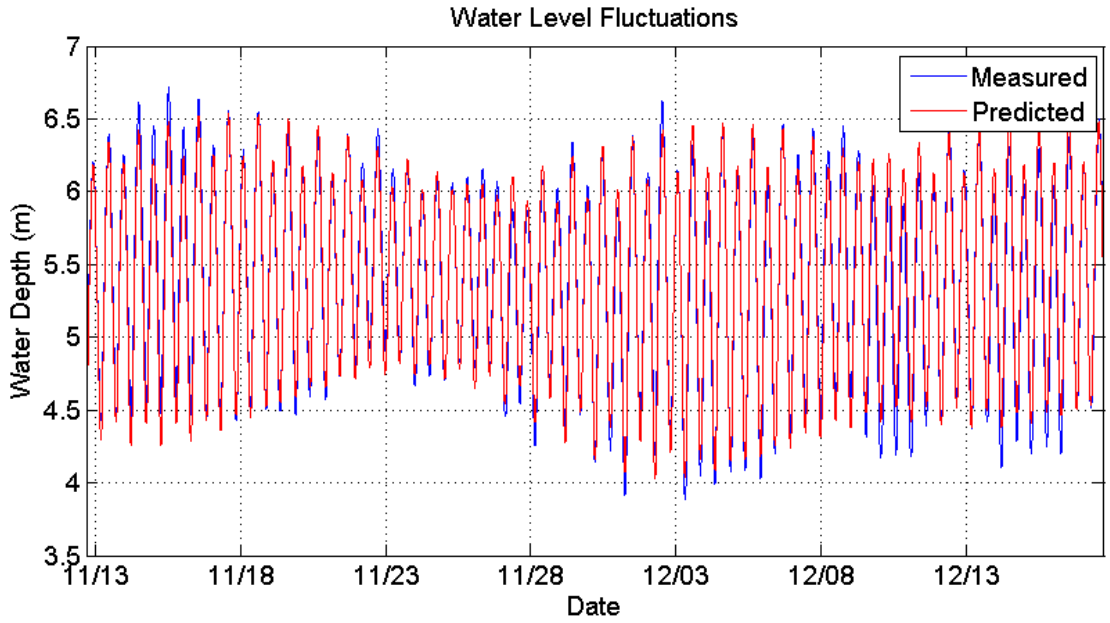

Figure 3.9. Time series of the water level fluctuations measured by the standalone ADCP compared to that predicted from the results of the tidal decomposition. Times are GMT.

Figure 3.10 is a comparison of the current velocities at the water surface measured by the ADCP to those predicted by the results of the tidal decomposition. The ADCP was set to measure the velocity within 0.5 meter vertical sections (bins). Data shown in Figure 3.9 was taken from the uppermost 0.5 meters of the water column (the surface bin). The surface bin was identified using depth measurements derived from pressure readings taken by the ADCP with each velocity measurement, and the fact that the height of each bin remained constant at 0.5 meters. The maximum measured current velocity in this top bin was slightly greater than 1.2 m/s. The two peaks in current velocity around November 15 and December 3, 2009 occur during spring tidal cycles, while the dips in current velocity around November 25 and December 11 are a result of neap tidal cycles. Throughout the measurement period, the predicted and measured current velocities are highly correlated and appear to be in phase. Only negligible differences in the two data sets occur at the points of maximum currents. The average magnitude of the difference between the measured and predicted values over the entire measurement period is 0.06 m/s. The predicted currents tend to slightly underestimate the actual velocity values, as expected, because the measured current velocities include flow from freshwater inputs which are not accounted for in the results from the tidal analysis. This indicates that the flow in the river is tidally dominated and the constituents account for the majority of the flow.

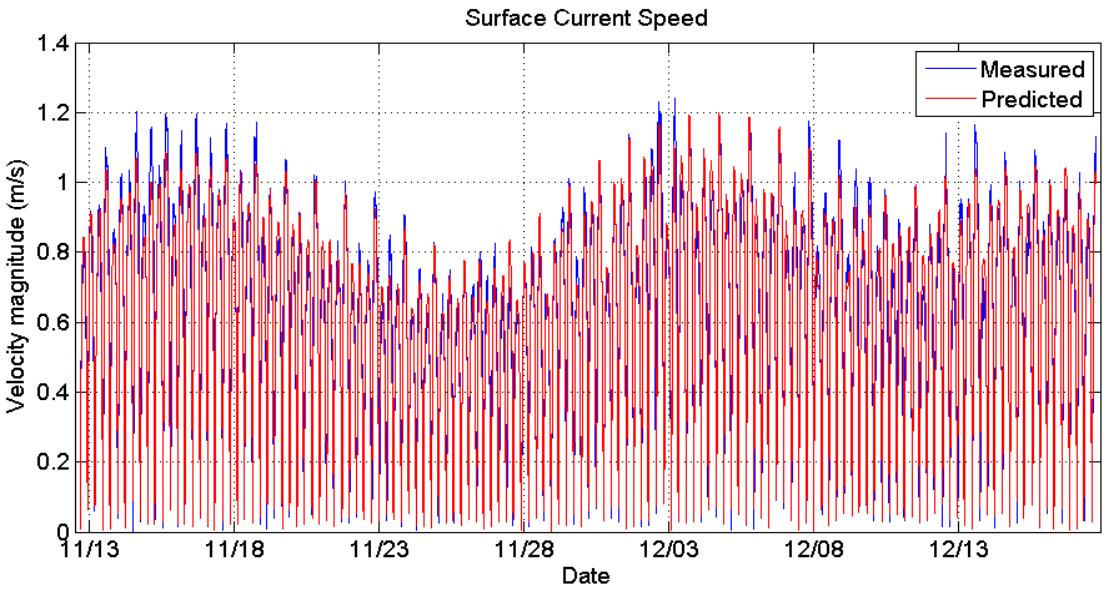

Figure 3.10. Time series of the current velocities at the water surface measured by the standalone ADCP compared to those predicted from the results of the tidal decomposition. Times are GMT.

Another comparison between measurements and predictions is presented in Figure 3.11. This figure shows a time series of the current velocity averaged over the entire water column (i.e. over all bins). Note that the maximum speed measured is slightly less than 1.2 m/s. Over the entire measurement period, it can be seen that the depth-averaged current speed is lower than the current speed at the surface. This result is typical of a boundary layer type vertical current profile which was observed at the site. Once again, both measurements and predictions match well; the average magnitude of the difference is 0.05 m/s over the entire measurement period. The kinetic energy contained in the flow at the ADCP location per meter width of channel computed from the measured depth-averaged current speed time series is 648 kW-hrs per month. Similarly, the same value computed using the results from the tidal analysis is found to be 638 kW-hrs per month. Therefore, approximately 98% of the kinetic energy in the flow at this location is tidally generated.

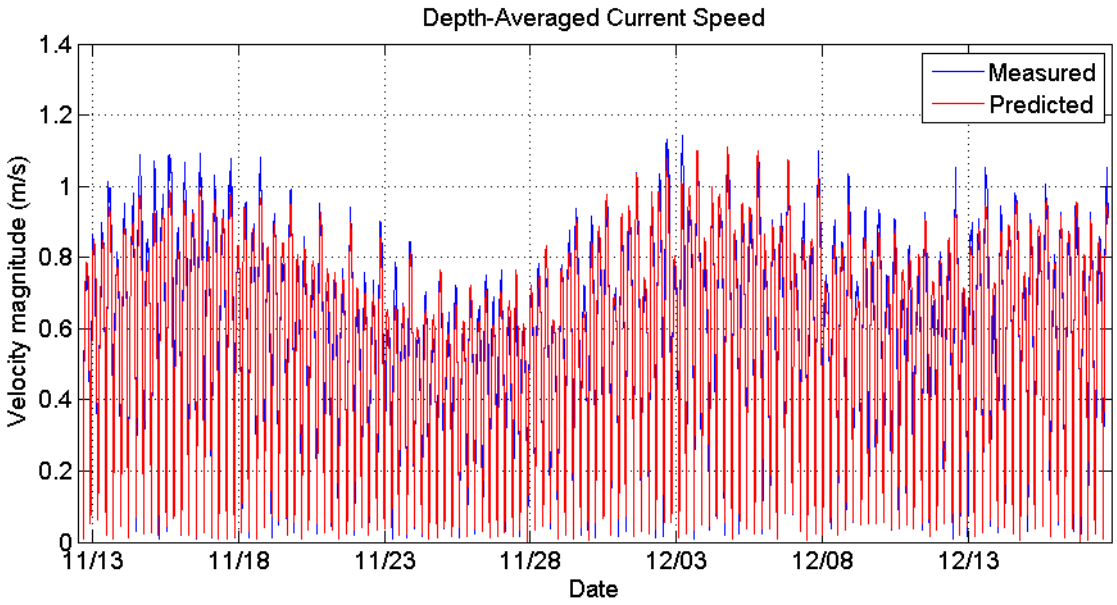

Figure 3.11. Time series of the depth-averaged current velocities measured by the standalone ADCP compared to that predicted from the results of the tidal decomposition. Times are GMT.

Current magnitude and power density histograms were developed for a time period of one year using the validated results from the tidal decomposition of the measured currents. The computed constituents were used to predict current velocities at the location of the ADCP over an entire year. Each histogram shows the distribution of the number of hours per year for the range of tidal current magnitudes and power densities at this location. In the upper histograms in Figures 3.12 and 3.13, the range of predicted current speeds was split up into 20 bins, using a bin size of about 6 cm/s. The number of hours per year that the current speed fell within each bin was then calculated and plotted.

The tidal power per unit flow cross-sectional area, or power density (P_{tide}), is calculated using the equation

$$P_{tide} = \frac{1}{2} \cdot \rho \cdot \left|\vec{V}\right|^3 \qquad (3.2)$$

where ρ is the water density (assumed to be constant at 1025 kg/m^3) and $|\vec{V}|$ is the current velocity magnitude. The lower histograms in Figures 3.12 and 3.13 were developed in a similar manner by splitting the range of power densities into 20 bins, each with a bin size of approximately 45 W/m^2. These histograms, along with dimensions of the proposed turbines, can be used to determine the available power in kW-hours per day or year, for example. The actual output power depends on the efficiency of the specific turbine.

Figure 3.12 shows current magnitude and power density histograms for the surface currents. The current magnitudes occurring most frequently throughout the year are approximately 0.75-0.85 m/s as shown in the upper histogram. There is a steady rise in the number of hours per year for each current speed up to 0.78 m/s, and a steady drop at current speeds above 0.84 m/s. The most frequently occurring power density is found in the smallest bin, between 0 and 45 W/m^2.

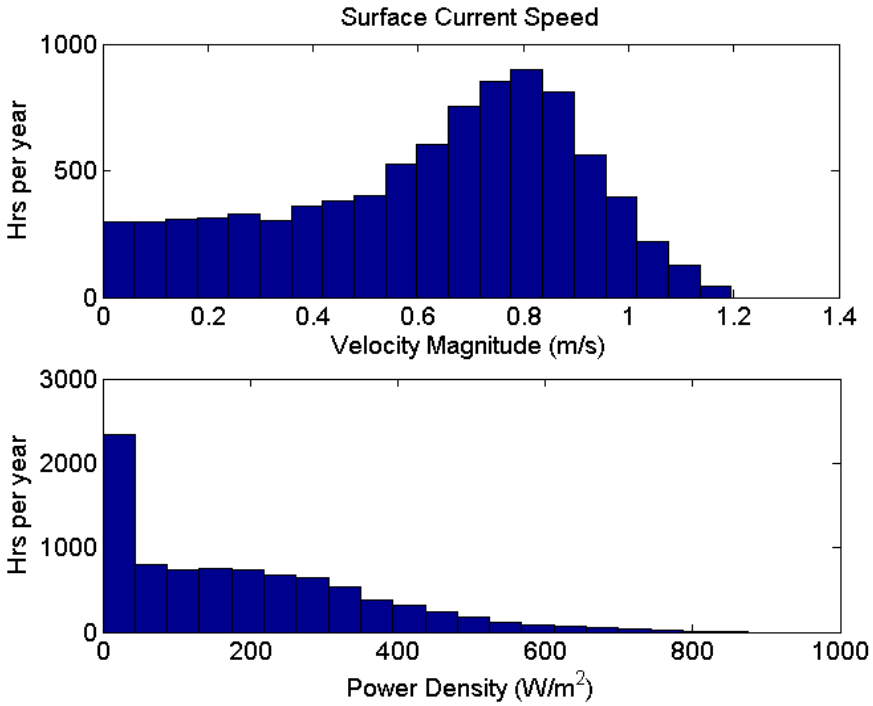

Figure 3.12. Histograms for the number of hours per year of the water surface current magnitude and power density.

Figure 3.13 shows depth-averaged current magnitude and power density histograms. The most frequently occurring depth-averaged current magnitude (0.70-0.75 m/s) is less than that at the water surface, which is a typical result. There is little change in the depth-averaged power density histogram versus the surface velocity histogram.

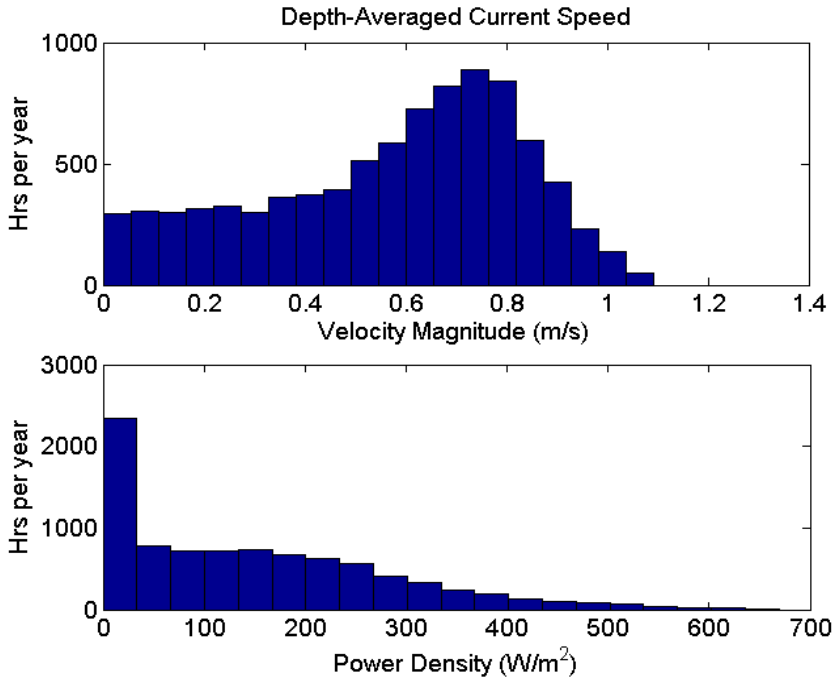

Figure 3.13. Histograms for the number of hours per year of the depth-averaged current magnitude and power density.

Results from in-situ measurements indicate that tidal currents along the portion of the Beaufort River analyzed in this study are driven primarily by the semi-diurnal M2 tidal constituent. The tidal range at the study site is approximately 2 meters on average, with a mean depth-averaged current velocity magnitude of 0.57 m/s predicted for a period of one year. This corresponds to a mean power density of 94.9 W/m^2 over the course of one year. The maximum current speed at the site is approximately 1.2 m/s at the water surface. Taking into account the relatively shallow water depth and moderate current velocities at this particular location, the generation of modest amounts of energy is

possible with the utilization of low-flow, possibly floating, turbines. For example, with a 10 m^2 intake area, a turbine with 50% efficiency would generate 8400 kW-hrs of power per year. This is about 76% of the 11,040 kW-hrs of power per year consumed by an average American household in 2008 (U.S. Energy Information Administration, 2010).

CHAPTER 4

NUMERICAL MODELING OF TIDAL CURRENTS

In addition to the field measurements presented in the previous chapter, the tidal currents in the vicinity of Parris Island, SC were assessed using the Regional Ocean Modeling System (ROMS). ROMS is a three dimensional, free-surface, terrain-following, numerical model which solves the Reynolds-averaged Navier-Stokes equations using the hydrostatic and Boussinesq approximations. Transport equations are used to solve momentum and scalar advection and diffusive processes, and an equation of state determines the density field accounting for temperature, salinity, and suspended-sediment concentration (Haidvogel et al., 2008; Shchepetkin and McWilliams, 2005). Multiple choices are available for many of the model components such as advection schemes, turbulence models, lateral boundary conditions, surface and bottom boundary layer submodels, air-sea fluxes, surface drifters, a nutrient-phytoplankton-zooplankton model, and a fully-developed adjoint model for computing model inverses and data assimilation (Haidvogel et al., 2008; Shchepetkin and McWilliams, 2005). ROMS has been used across a variety of space and time scales for various purposes in marine modeling systems (Haidvogel et al., 2008; Shchepetkin and McWilliams, 2005). It has also previously been utilized to perform tidal simulations (Robertson, 2006; Xiaochun et al., 2006; Haidvogel et al., 2008; Defne et al., 2008).

The model was run to match the dates of the in-situ ADCP deployment from November 12 to December 17, 2009 and was calibrated using the measurements presented in Chapter 3. Results from the model allow for a better spatial observation of the currents in the Beaufort River in the vicinity of the study area. The model was also used to simulate the effect of energy extraction on the local flow field by including an

additional dissipation term at the locations of the extraction devices, the results of which will be discussed in the next chapter.

4.1 Model Setup

The grid used by the ROMS model in this study was adapted from an existing grid created by Lide Jiang at Georgia Tech Savannah. The pre-existing grid consisted of 802 grid cells in the longshore direction and 202 grid cells in the cross-shore direction (see Figure 4.1). Each grid cell represents a 200 m by 200 m square portion of the coast. Numerous rows of grid cells were truncated in the longshore direction on both the Southern and Northern portions of the existing grid. The grid width in the cross-shore direction remained unchanged. The final product was a 202 by 212 cell grid centered about Parris Island, SC (see Figure 4.2). The color scale in Figures 4.1 and 4.2 indicates the water depth in meters, with red indicating deeper water.

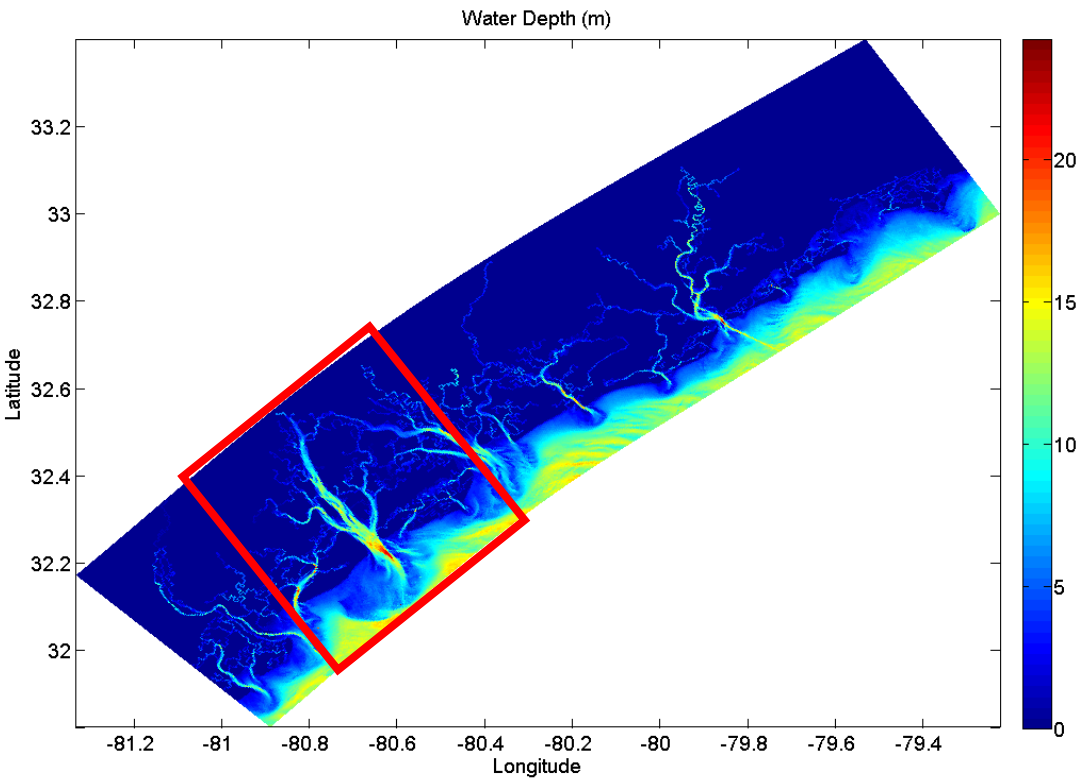

Figure 4.1. Full grid used in the ROMS model applied to most of the South Carolina coast by Lide Jiang at Georgia Tech Savannah. The color scale indicates the water depth in meters and the red box indicates the area covered by the truncated ROMS grid.

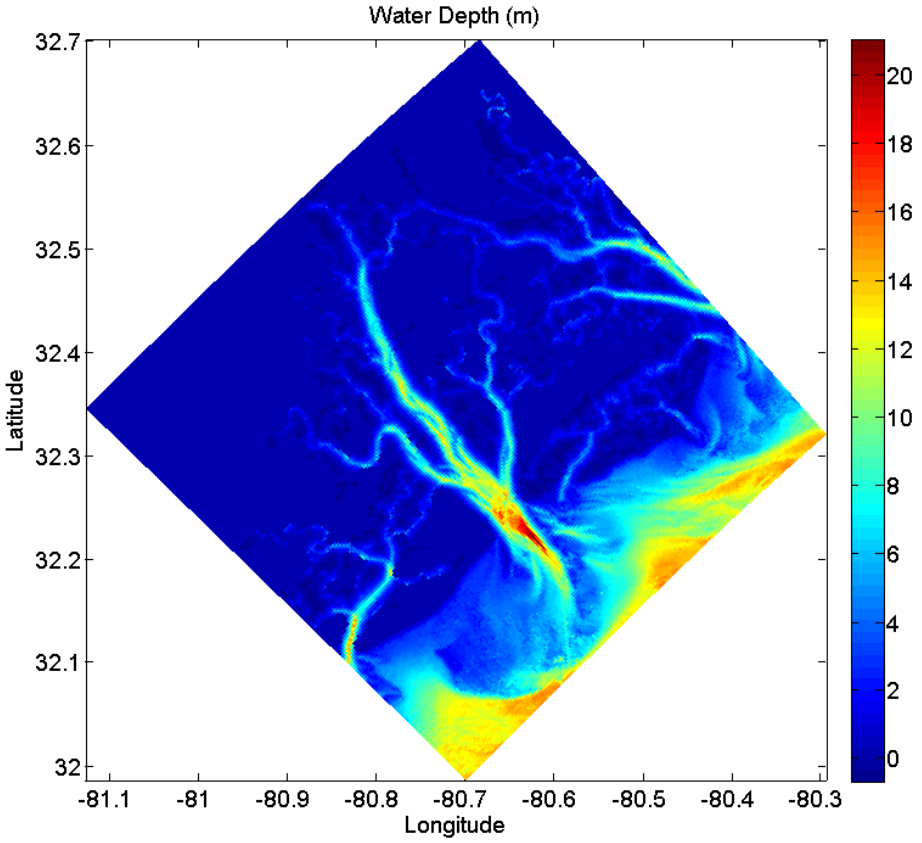

Figure 4.2. Truncated grid used in the ROMS model applied to Parris Island, SC and surrounding areas. The color scale indicates the water depth in meters.

Figure 4.3 displays a more detailed view of the central portion of the ROMS grid in the vicinity of Parris Island. The white box outlines the approximate area analyzed during the boat-based survey and the yellow "x" indicates the location of the in-situ ADCP deployment discussed in the previous chapter. With this grid resolution, the area of interest in this study is comprised of approximately four grid cells in the cross-channel direction, and seven grid cells in the along-channel direction.

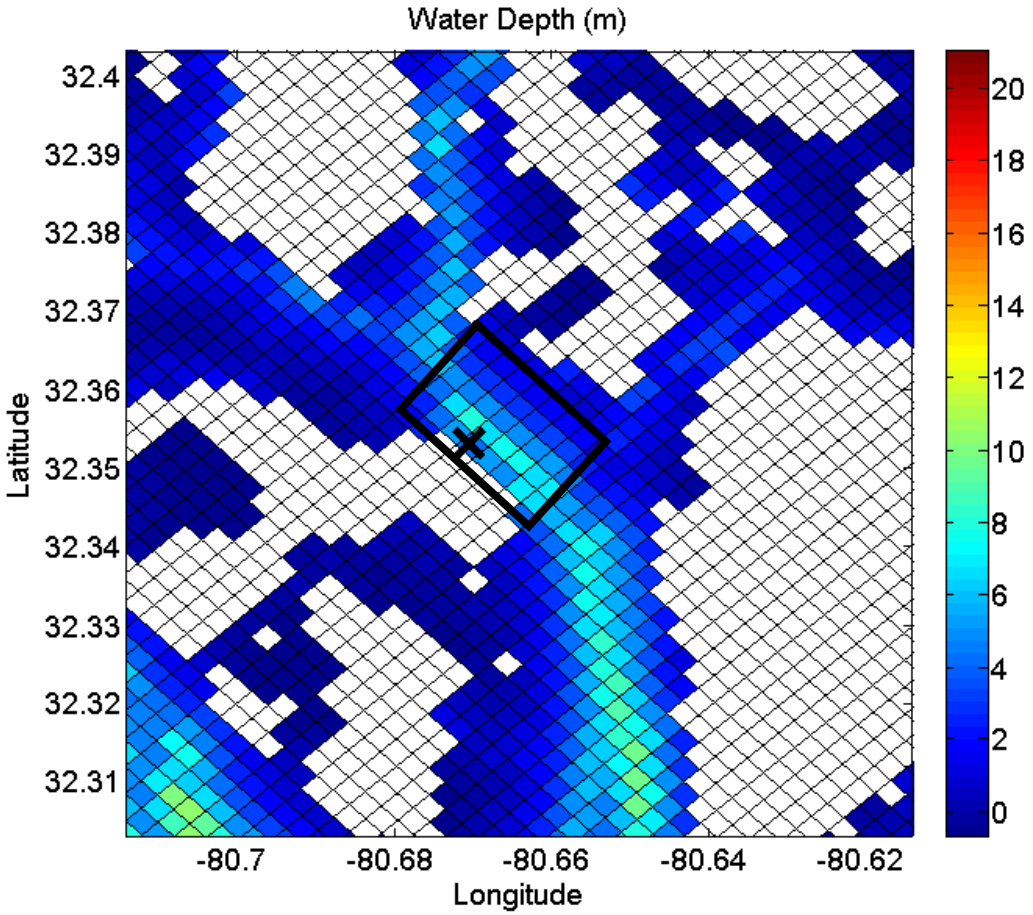

Figure 4.3. Close-up of the Parris Island, SC area within the ROMS grid with the approximate area of interest in this study outlined by the black box and the location of the in-situ ADCP deployment denoted with a black "x". The color scale indicates the water depth in meters and white cells indicate land.

Coastline and bathymetry data used throughout the model domain was obtained from the National Geophysical Data Center (NGDC). The coastline extractor available at the NGDC website (NGDC, 2008) was used to extract the coastline dataset, and the bathymetry data was downloaded through the ArcIMS interface provided by NGDC, the official source for National Ocean Service (NOS) bathymetric maps (NOS, 2008). The vertical datum for the bathymetry data was adjusted using the Mean Lower-Low Water (MLLW) and Mean Tidal Level (MTL) values reported by NOAA at the local tidal stations, and then used to generate depths within each grid cell. The version of the

ROMS used in this study uses eight vertical terrain-following layers for model computations.

The wetting and drying of wetlands within the computational grid are simulated in ROMS by specifying a "critical depth" for these grid cells. For a wetland grid cell to become submerged during a flood tidal cycle, the elevation of the water surface must rise above the specified elevation of the wetland grid cell plus the critical depth. The depths of the grid cells designated as wetlands are negative with a value of -0.5 meters in this study, whereas, grid cells that remain submerged have positive depth values. The critical depth in the wetland cells was set to 10 cm in this study, therefore, the mean water level must reach 60 cm for the wetland cells to become submerged.

The model uses the predicted tidal forcing along the seaward boundaries of the grid to produce simulations of the tidal currents throughout the model domain. The tidal forcing used in this version of the ROMS model was obtained from the ADCIRC tidal database created by the numerical model ADCIRC for the Western North Atlantic Ocean (Mukai et al, 2002). Tidal constituents used from this database include the M2, S2, N2, K2, O1, K1, P1, and Q1 components. These constituents were extracted from the tidal database and applied at the open boundary of the computational grid forcing the ROMS tidal current simulations.

4.2 Model Results

Prior to running the ROMS model, the location of the in-situ ADCP deployment (32° 21.191' N, 80° 40.228' W) was designated as a station in one of the model input files. For each designated station, the ROMS model will output a more detailed set of results at that exact location. This data set was compared to the actual measurements taken by the ADCP during the longer-term deployment discussed in the previous section. The station location within the grid is indicated in Figure 4.3 by the yellow "x". The ROMS model was run to match the times of the in-situ ADCP deployment discussed in

Chapter 3. This was a 35 day period extending from November 12 to December 17, 2009. In order to eliminate the effects of model spin-up time, the model was set to begin on November 9, 2009, three days prior to the in-situ measurement start date. Model results from November 9 to November 11, 2009 were then discarded. After calibration, the dimensionless bottom friction factor was set to 0.001 to produce accurate agreement between the modeled and measured current velocity magnitudes. A 30 s time step was used for model calculations, resulting in a total computational time of about 18 hours using 4 processors. Results output by the model at the location of the in-situ ADCP measurements are presented below.

The fluctuations in water surface elevation (ζ) about the mean water level predicted by the ROMS model at the ADCP deployment location are compared to actual measurements in Figure 4.4. As seen in the figure, the two time series match closely after November 27. Before this point, the modeled water level fluctuations are consistently lower than the actual values by approximately 0.5 m. A maximum difference in water surface fluctuation of about 0.6 m is observed throughout the entire measurement period. The average MWL's predicted by the model and measured by the ADCP over the entire measurement period are 5.63 m and 5.14 m, respectively. This offset is due to the bathymetry data and course resolution used in the ROMS grid.

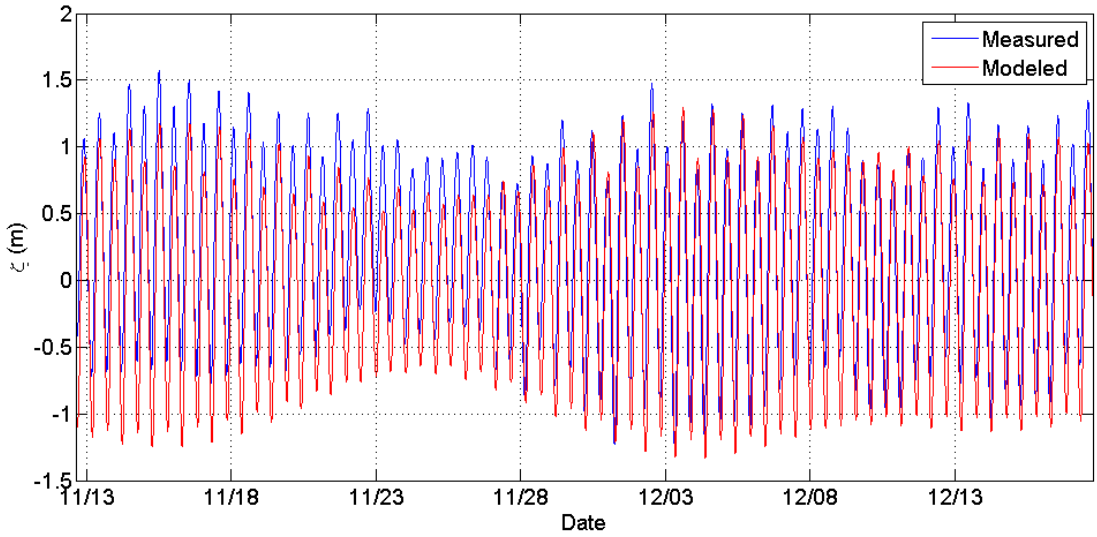

Figure 4.4. Time series of the fluctuations in water level about the MWL predicted by the final version of the ROMS model compared to in-situ measurements taken by the ADCP.

Figure 4.5 is a comparison between the time series of the surface current velocity magnitude output by ROMS model and the times series developed using in-situ measurements taken during the longer-term ADCP deployment. The blue line represents the surface current velocity measured by the ADCP over the longer-term deployment. The red line shows the surface current velocity predicted by the model at the same location. The modeled and measured time series are very similar in current velocity magnitude, but differ slightly in phase. The model also reproduces the actual spring-neap tidal cycle observed at the site. The maximum measured surface current speed is 1.24 m/s, while the maximum surface current speed predicted by the model is 1.15 m/s.

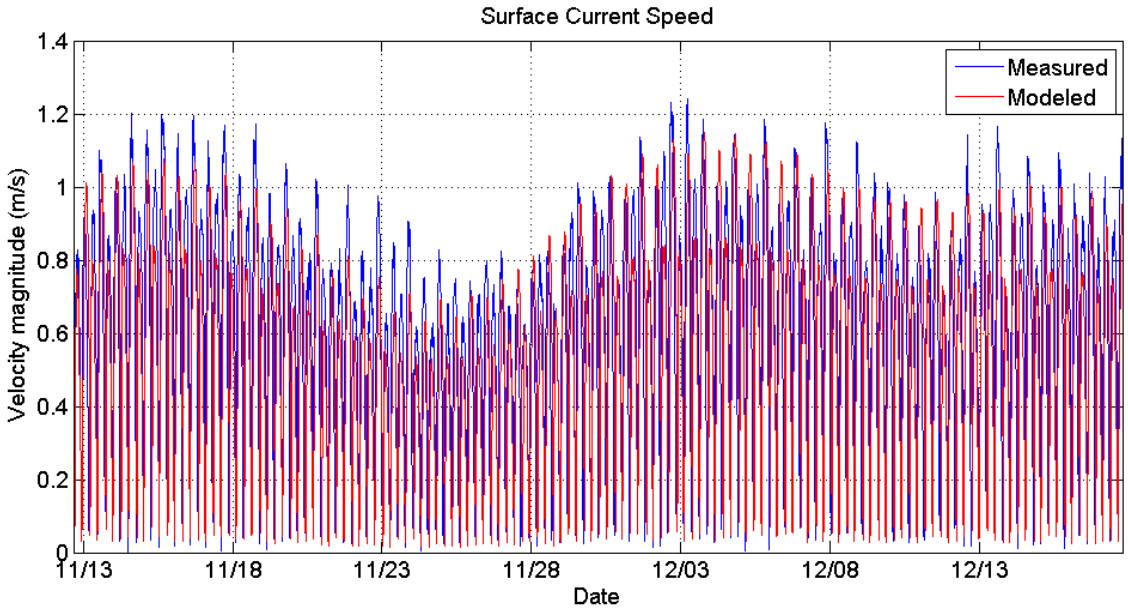

Figure 4.5. Time series of the surface current velocity magnitude output by ROMS model compared to in-situ measurements taken during the longer-term ADCP deployment.

A similar comparison to that in Figure 4.5 can be made between the modeled and measured depth-averaged current velocity magnitudes (Figure 4.6). The same trends observed in the surface current speed time series can be seen in the depth-averaged current speed time series. The modeled and measured results are alike in magnitude, but are slightly out of phase. The maximum modeled depth-averaged current velocity magnitude is 1.08 m/s which only differs from the maximum measured value of 1.14 m/s by 6 cm/s.

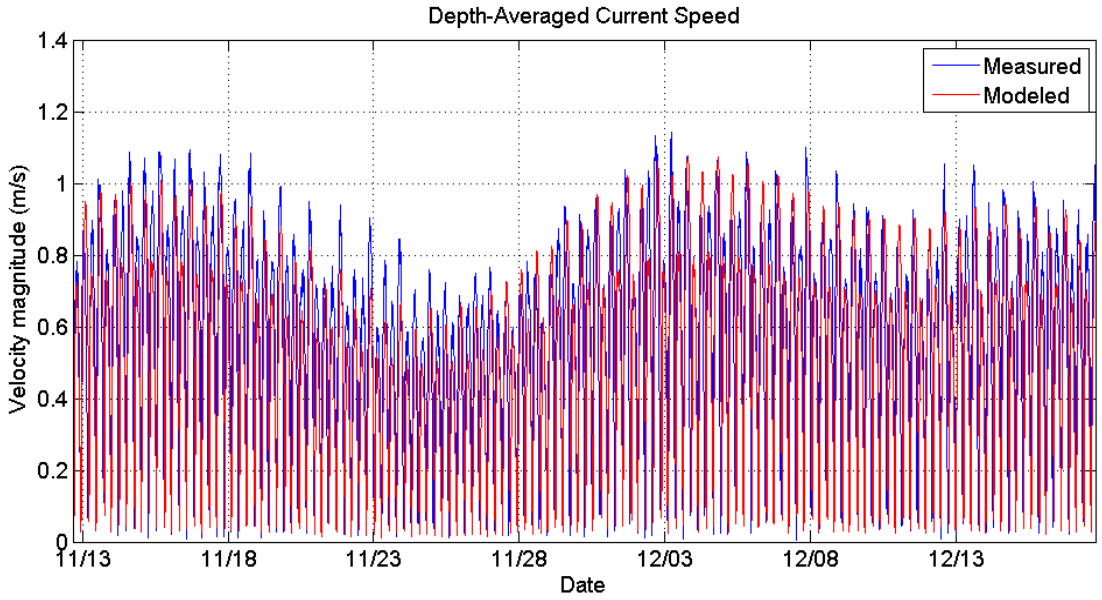

Figure 4.6. Time series of the depth-averaged current velocity magnitude output by ROMS model compared to in-situ measurements taken during the longer-term ADCP deployment.

A quantification of the differences between the modeled and measured currents is presented in Table 4.1. In Equations 4.1 through 4.7, the i^{th} occurrence and total number of occurrences of maximum and minimum during the simulation period are denoted by i and N, respectively. The Mean Current Magnitude Ratio of Maximum Currents (*cmgrt*) is the average ratio of the maximum current speeds from the model to the corresponding maximum current speeds from the measured data. This parameter includes both flood and ebb tidal currents, and is calculated using the equation

$$cmgrt = \frac{\sum_{i=1}^{N} \frac{|(cur_m)_i|}{|(cur_v)_i|}}{N} \tag{4.1}$$

where cur_m is the local maximum current velocity magnitude from the model and cur_v is the local maximum current velocity magnitude from the measured data.

The Root-Mean-Square Difference of Maximum Currents (*crms*) is the root-mean-square of the difference between the maximum current speeds output by the model and those measured at the site, and is given by

$$crms = \sqrt{\frac{\sum_{i=1}^{N}\{(cur_m)_i-(cur_v)_i\}^2}{N}} \tag{4.2}$$

where each variable represents the same parameter found in Equation 4.1.

The Root-Mean-Square Difference of Maximum Flood and Ebb Currents (*fcrms* and *ecrms*) are calculated using the same equation as Equation 4.2, but only the maximum flood or ebb current speeds are considered. The Mean Differences in Maximum Flood and Ebb Currents (*fcmd* and *ecmd*) are simply the mean differences in the maximum flood or ebb current speeds between the model and measurements. They are found using the following equations:

$$fcmd = \frac{\sum_{i=1}^{N}\left\{\left(cur_m^f\right)_i-\left(cur_v^f\right)_i\right\}}{N} \tag{4.3}$$

and

$$ecmd = \frac{\sum_{i=1}^{N}\{(cur_m^e)_i-(cur_v^e)_i\}}{N} \tag{4.4}$$

where cur_m^f and cur_v^f are the maximum modeled and measured flood currents, respectively, and cur_m^e and cur_v^e are the maximum modeled and measured ebb currents, respectively. The values calculated for *fcmd* and *ecmd* are greater than zero if the modeled current speed is larger than the measurements and less than zero if the modeled current speed is smaller than the measurements. They are used to assess the ability of the model to simulate the flood or ebb dominant tidal regimes.

Finally, the Phase Difference Between Maximum Currents (*cpd*) is the mean phase difference between the modeled and measured maximum current speeds, and is given by

$$cpd = \frac{\sum_{i=1}^{N}\{(t_m)_i-(t_v)_i\}}{N} \tag{4.5}$$

Where t_m and t_v are the times corresponding to the maximum tidal current occurrences in the model output and the measured data, respectively. The Phase Differences Between Maximum Flood and Ebb Currents (*fcpd* and *ecpd*) are calculated similarly using only the flood and ebb current speeds, and are given by

$$fcpd = \frac{\sum_{i=1}^{N}\left\{\left(t_m^f\right)_i - \left(t_v^f\right)_i\right\}}{N} \tag{4.6}$$

and

$$ecpd = \frac{\sum_{i=1}^{N}\{(t_m^e)_i - (t_v^e)_i\}}{N} \tag{4.7}$$

where the superscripts *f* and *e* denote flood and ebb, respectively. The values calculated for *cpd*, *fcpd*, and *ecpd* are greater than zero if the modeled phase output lags the measured data and less than zero if the modeled phase output leads the measured data.

A *cmgrt* of 0.95 was calculated from the modeled and measured current velocity time series, in other words, the average of the modeled maximum currents is 95% of that measured. The modeled current velocities for the ebb tidal cycles match the measured velocities more closely than during the flood tidal cycles, on average, as indicated by the values calculated for *fcrms* and *ecrms*, and *fcmd* and *ecmd*. The *cpd* was calculated to be +13.8 minutes, which indicates that the modeled current velocity phase lags the measured data by a relatively small amount, considering that tidal variations occur over time periods of several hours. The negative value of the *fcpd* indicates that the maximum modeled flood currents lead the maximum measured flood currents by an average of 29.6 minutes. Conversely, the positive value of the *ecpd* means that the maximum modeled ebb currents lag the measurements by an average of 63.2 minutes.

Table 4.1. Statistical comparison between modeled vs. measured tidal currents.

Mean Current Magnitude Ratio of Maximum Currents	*cmgrt*		0.95
Root-Mean-Square Difference of Maximum Currents	*crms*	**m/s**	0.081
Root-Mean-Square Difference of Maximum Flood Currents	*fcrms*	**m/s**	0.090
Root-Mean-Square Difference of Maximum Ebb Currents	*ecrms*	**m/s**	0.070
Mean Difference in Maximum Flood Currents	*fcmd*	**m/s**	-0.070
Mean Difference in Maximum Ebb Currents	*ecmd*	**m/s**	-0.015
Phase Difference Between Maximum Currents	*cpd*	**minutes**	13.8
Phase Difference Between Maximum Flood Currents	*fcpd*	**minutes**	-29.6
Phase Difference Between Maximum Ebb Currents	*ecpd*	**minutes**	63.2

After calibrating the current velocity magnitude results for the ROMS model using the measurements, a tidal decomposition was performed on both the modeled current velocity and mean water level time series. The Matlab toolbox "T-Tide" (Pawlowicz et al, 2002) was used to perform a harmonic analysis of both the modeled depth-averaged current velocity magnitude and mean water level time series. The results from the harmonic analysis of the modeled time series are compared to that from the measurements in Table 4.2. Again, the site is found to be dominated by the semi-diurnal M2 tidal constituent, which is caused by the gravitational force from the moon. The modeled M2 water level amplitude differs from the actual M2 water level amplitude by only 7 cm, and the modeled M2 velocity amplitude is a mere 8.7 cm/s less than the actual. Other significant modeled tidal constituents also show minimal differences in these parameters. Differences in the modeled and measured constituents are most evident in the water level and velocity phases, which are of less importance for the purposes of this study.

Table 4.2. Depth-averaged M2, N2, K1, and S2 tidal constituents and their properties derived from the ROMS model and fixed ADCP velocity and stage measurements. Velocity inclination corresponds to compass heading of major axis of tidal ellipse.

Constituent			M2	N2	K1	S2
Frequency	**hr^{-1}**	**Modeled**	0.0805	0.0790	0.0418	0.0833
		Measured	0.0805	0.0790	0.0418	0.0833
Water Level Amplitude	**m**	**Modeled**	0.93	0.20	0.11	0.12
		Measured	0.86	0.19	0.12	0.11
Water Level Phase	**degrees**	**Modeled**	52.6	44.7	217.8	69.8
		Measured	31	26.4	204.9	52.5
Velocity Amplitude	**m/s**	**Modeled**	0.785	0.158	0.049	0.101
		Measured	0.872	0.176	0.065	0.106
Velocity Phase	**degrees**	**Modeled**	335.3	330.0	124.5	355.8
		Measured	318.3	311.1	120.1	347.6
Velocity Inclination	**degrees**	**Modeled**	129.8	129.3	130.0	129.3
		Measured	120.0	119.2	119.4	120.6

The spatial variation in the currents predicted by the ROMS model in the absence of energy extraction devices is of particular interest so that comparisons can be made to the case in which extraction devices are present. Figure 4.7 displays the variation in the mean and maximum current magnitudes predicted by the model over the full simulation time period in the vicinity of Parris Island. The mean current magnitude near the location of the ADCP station is about 0.45 m/s, while the maximum current magnitude is about 1.0 m/s. Stronger currents are predicted by the model along the southwestern edge of the study site, which is consistent with the actual measurements presented in Chapter 3. The strongest currents in the Beaufort River predicted by the model occur to the southeast of the study area, on the eastern side of Parris Island.

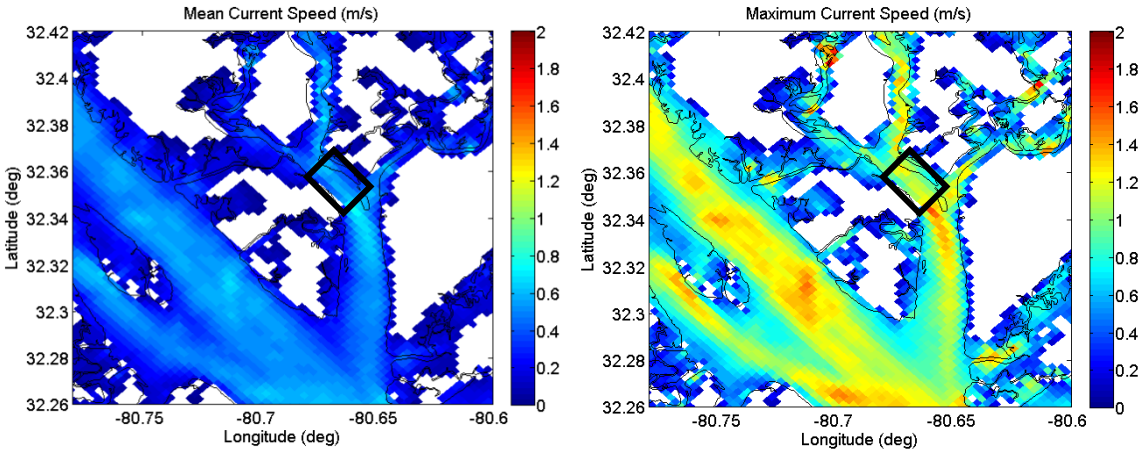

Figure 4.7. Spatial variation in mean current magnitude (left) and maximum current magnitude (right) predicted by the ROMS model between November 12 and December 17, 2009. The approximate area of interest in this study is outlined by the black box.

The spatial variation in power density in the vicinity of Parris Island in the absence of energy extraction devices in displayed in Figure 4.8. The spatial power density follows the same trends of current speed observed in Figure 4.7. A relatively low mean power density of around 200 W/m^2 and a maximum power density of about 1000 W/m^2 were predicted by the model near the ADCP location.

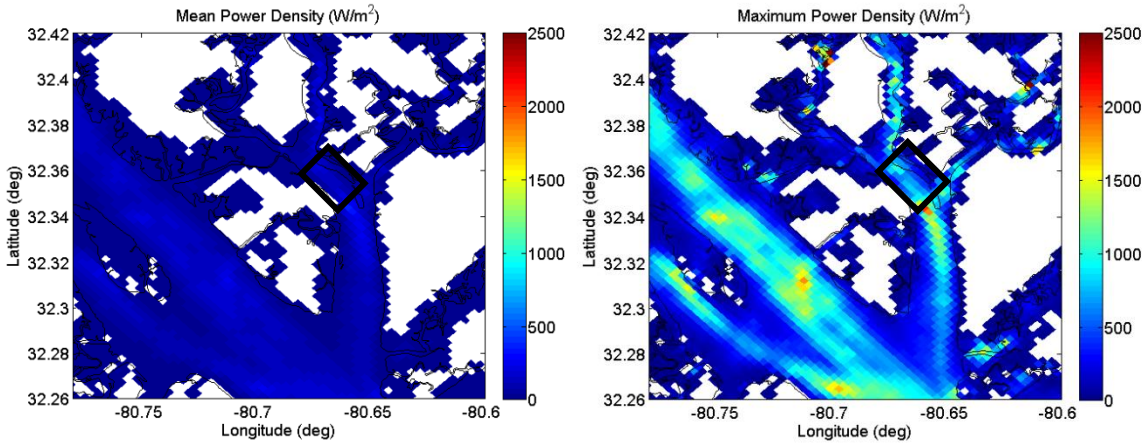

Figure 4.8. Spatial variation in mean power density (left) and maximum power density (right) predicted by the ROMS model between November 12 and December 17, 2009. The approximate area of interest in this study is outlined by the black box.

The spatial variation in the instantaneous depth-averaged current speeds throughout the study area is depicted in Figure 4.9. These images were taken from the model run on November 16, 2009 during the flood and ebb tidal cycles at 11:00 GMT and 17:00 GMT, respectively. The patterns observed in the in-situ current velocity measurements taken during the boat-based survey presented in Figures 3.6 and 3.7 are accurately reproduced by the ROMS model. Current speeds are higher on the Parris Island side of the Beaufort River during both tidal cycles, and decrease with distance across the channel. Current speeds are also higher during the ebb tide, as observed in the in-situ measurements. At the location of the ADCP deployment, the instantaneous current speed is approximately 0.5 m/s during the flood tide and 1.0 m/s during the ebb tide. These values also agree well with the in-situ measurements.

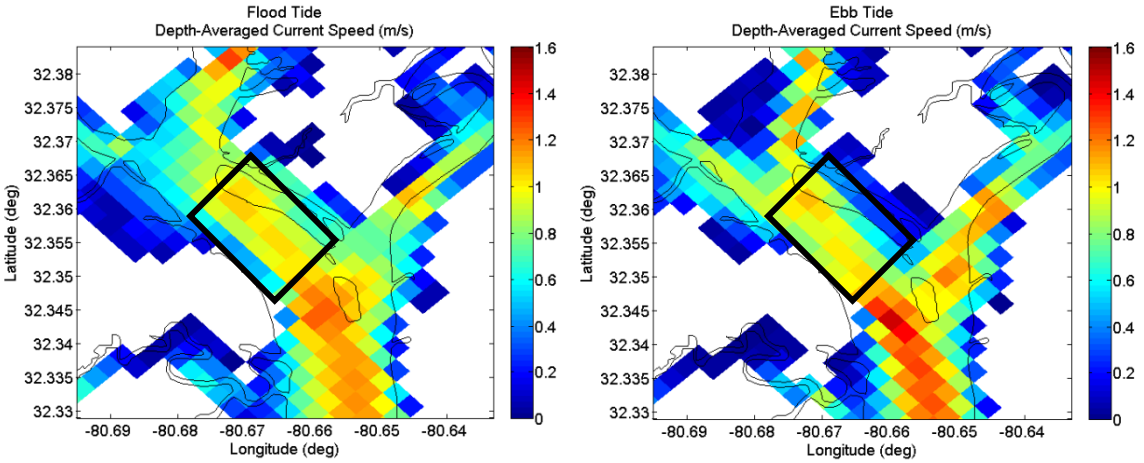

Figure 4.9. Spatial variation in depth-averaged current speed throughout the study site from the model run on November 16, 2009 during the flood tidal cycle at 11:00 GMT (left) and the ebb tidal cycle at 17:00 GMT (right). The approximate area of interest in this study is outlined by the black box.

The ROMS model applied to the coastal areas surrounding Parris Island, SC produces results that closely resemble in-situ measurements collected previously during both the boat-based survey and the longer-term ADCP deployment. Although the modeled water level phase differs significantly from the measurements by 13.8 minutes on average, this is a relatively insignificant difference considering that tidal variations occur over the course of several hours. The modeled current velocities are reasonable compared to measurements, and are of more importance. Maximum current velocities predicted by the model are within 5% of those observed in the field. Furthermore, spatial variations in current speed and power density agree well with in-situ measurements. Therefore, this version of the model can now be used to simulate the effects of the placement of underwater turbines on the surrounding environment in Chapter 5.

CHAPTER 5

MODELING OF THE IMPACT OF ENERGY EXTRACTION ON THE FLOW FIELD

Removing energy from any tidal flow will alter both the near-field and far-field flow patterns, to a certain degree. The severity of these effects depends on the amount of energy removed from the original, undisturbed flow. Recent studies suggest that the total amount of energy dissipation caused by the power converters be limited to 15-30% of the total power contained in the existing flow (Bryden et al., 2004; Couch and Bryden, 2006; Hagerman et al., 2006c; Polagye et al., 2008). The ROMS model discussed in previous chapters is used to simulate the impacts of energy extraction on the flow field in the vicinity of Parris Island, SC. The methodology used to model the effects of energy extraction on the hydrodynamics within the ROMS model will be discussed briefly, followed by an analysis of the model results for four different scenarios.

5.1 Modeling Energy Extraction

The effect of power extraction from the tidal flow is simulated by introducing an additional sink term into the governing momentum equations in the grid cells containing the extraction devices. The derivation of this sink term (from Defne et al., 2010) begins by defining a retarding force collinear with the direction of the flow as

$$\vec{F} = -\frac{P_{ext}}{|\vec{V}|} \cdot \frac{\vec{V}}{|\vec{V}|} \tag{5.1}$$

where $\vec{F}$ is the retarding force per unit surface area, $\vec{V}$ is the flow velocity vector, $|\vec{V}|$ is the magnitude of the flow velocity vector, and P_{ext} is the extracted power density given by

$$P_{ext} = C_{ext} \cdot P \tag{5.2}$$

where C_{ext} is the extraction coefficient and P is the power per unit area in the flow given previously in Equation 3.2. To obtain the sink terms that are substituted into the governing equations in x and y, Equations 5.1 and 5.2 are combined to obtain

$$F_u = -C_{ext} \cdot \frac{1}{2} \cdot \rho \cdot u \cdot \left|\vec{V}\right| \tag{5.3}$$

$$F_v = -C_{ext} \cdot \frac{1}{2} \cdot \rho \cdot v \cdot \left|\vec{V}\right| \tag{5.4}$$

where ρ is the water density, u and v are the velocity components in the x and y directions, respectfully, F_u and F_v are the retarding force components per unit surface area.

The total power dissipated (P_{diss}) from the flow field includes the power extracted as well as any other losses and is found as

$$P_{diss} = P_{ext} \cdot dx \cdot dy \tag{5.5}$$

where dx and dy are the grid cell dimensions in the x and y directions, respectively.

The total available kinetic power within a channel cross-section is defined as

$$P_{avail} = \sum_{i=1}^{N} \frac{1}{2} \cdot \rho \cdot \left|\vec{V}\right|^3 \cdot h \cdot w \tag{5.6}$$

where h and w are the depth and width of each of the grid cells across the channel, and N is the total number of cells across the channel. The value of P_{avail} across the channel at the extraction location analyzed in this study is 610 MW-hrs per month.

Four different cases will be analyzed using results from the model simulation. In Case 1, 10% of the total kinetic energy contained in the flow cross-section is extracted from one grid cell at the location of the longer-term ADCP deployment discussed in Chapter 3. Cases 2, 3, and 4 correspond to scenarios in which 20, 30, and 60% of the total kinetic energy is extracted from two grid cells in the same cross-section as in Case 1, respectively. Extraction was simulated in two grid cells for cases 2 through 4 because the grid cell used in Case 1 contains only 13.6% of the total kinetic energy in the channel cross-section. Therefore, the energy extracted from this cell alone can never account for over 13.6% of the total kinetic energy in the channel cross-section. For each case, the

impacts of energy extraction will be evaluated by examining the change in current velocity, power density, and water level in the model domain before and after extraction.

5.2 Case 1: 10% Kinetic Energy Extraction

Case 1 corresponds to the scenario in which approximately 10% of the total kinetic energy contained in the channel cross-section at the extraction location is dissipated from the flow by the energy extraction devices. For this case, an extraction coefficient (C_{ext}) of 0.2 was used in the grid cell at the location of the longer-term ADCP deployment discussed in Chapter 3. The spatial difference in mean power density between Case 1 and the undisturbed flow case over the entire 35 day time period are shown in Figure 5.1. The difference in mean power density is a maximum in the grid cell containing the simulated extraction devices. A deficit in power density of about 70 W/m^2 occurs at this location. The effects of extraction are more pronounced downstream from the extraction location, since larger current speeds develop during the ebb tidal cycle at this location. An increase in power density is observed throughout the remainder of the channel cross-section, as a fraction of the flow is redirected around the extraction devices. In this case, the far-field effects (> 1 km away) of energy extraction are minimal.

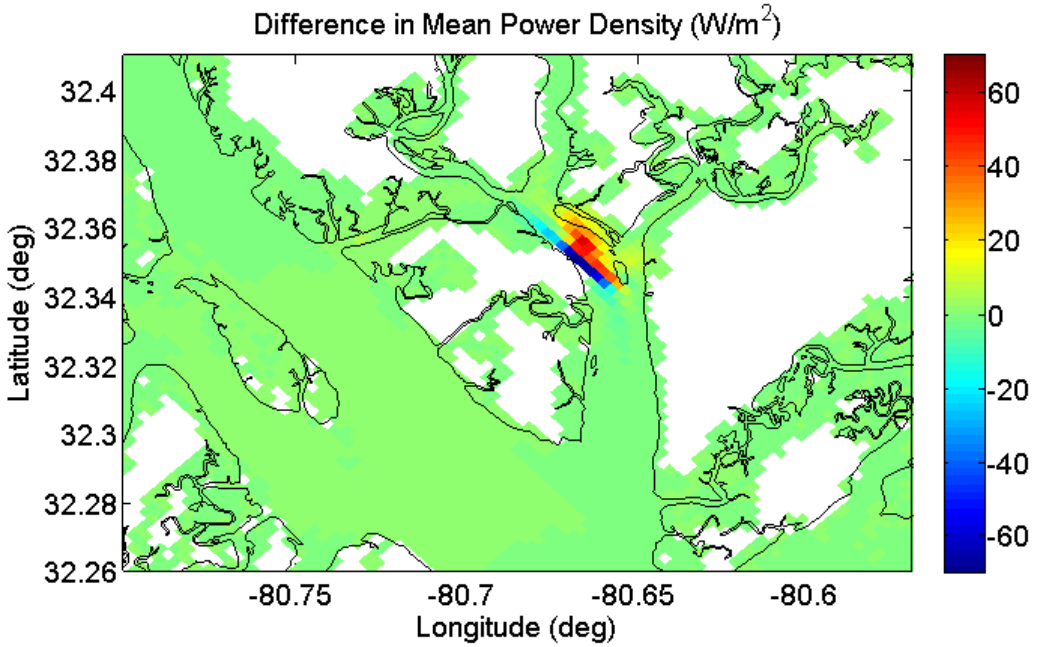

Figure 5.1. Spatial difference in mean power density between the undisturbed flow case and the case with 10% kinetic energy extraction.

Figure 5.2a shows the spatial difference in mean current speed between Case 1 and the undisturbed flow case over the entire 35 day time span. Again, it can be seen that the maximum difference in the current speed occurs in the grid cell containing the extraction devices. At this location, the currents are reduced by approximately 0.3 m/s. Current speeds are also reduced directly upstream and downstream from the extraction location, with a more noticeable reduction downstream. Current speeds are amplified throughout the remainder of the channel cross-section, as seen previously in Figure 5.1.

Figures 5.2b and 5.2c display time series of the depth-averaged current speed at one point upstream from the extraction location (Station A) and at another point downstream of the extraction location (Station B) from December 3 to 6, 2009. These dates were chosen because the differences in the modeled current velocities were greatest during this time frame. In Case 1, the depth-averaged currents are consistently lower than the undisturbed flow case. The maximum difference in the peak depth-averaged current speeds at both stations is about 10 cm/s. A greater reduction in the current speed

occurs during each ebb tidal cycle, which is in agreement with the patterns displayed in Figure 5.2a.

Similarly, the mean water levels are presented in Figure 5.3. The spatial change in the maximum water level elevation observed over the 35 day model run between the undisturbed flow case and Case 1 is displayed below in Figure 5.3a. These changes are minimal for this case, on the order of one millimeter. However, the elevation of the maximum water level is most affected upstream from the extraction location in the Beaufort River. Downstream of the extraction location, the change in water level is reduced, although a general decrease is still observed. The time series at stations A and B reveal that at each low tide, the mean water level is slightly higher in Case 1 over this 3-day time period. However, at each high tide, the water level for Case 1 is slightly lower than the undisturbed flow case. These changes are minimal, about 10 cm maximum at low tide. The mean water level phase is also weakly affected by the presence of the extraction devices. In Case 1, the changes in water level are slightly lagging the no extraction case at both stations.

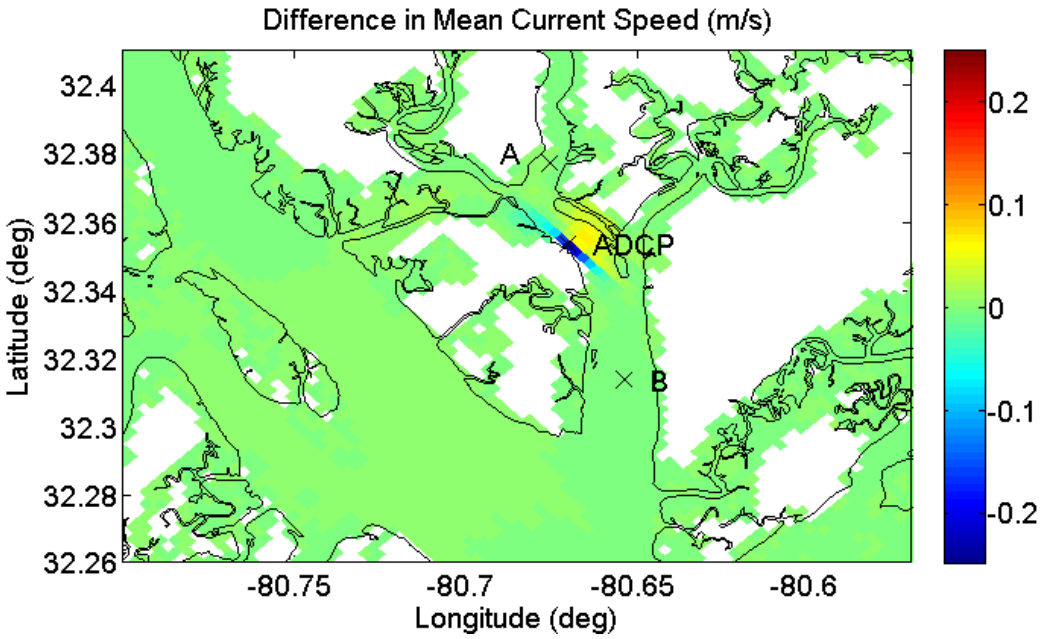

(a)

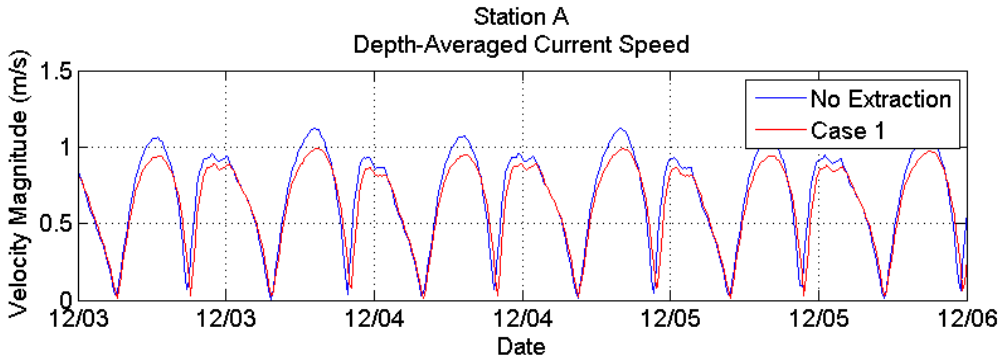

(b)

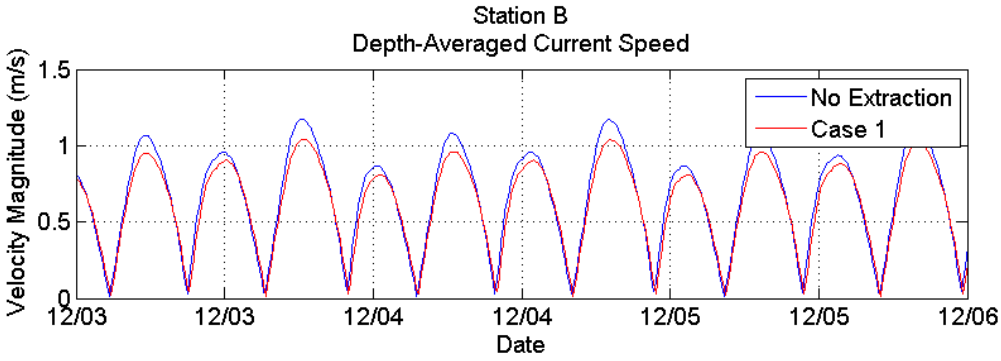

(c)

Figure 5.2. (a) Spatial difference in mean power density between the undisturbed flow case and the case with 10% kinetic energy extraction. Time series of depth-averaged current speed at locations (b) upstream and (c) downstream of the extraction location.

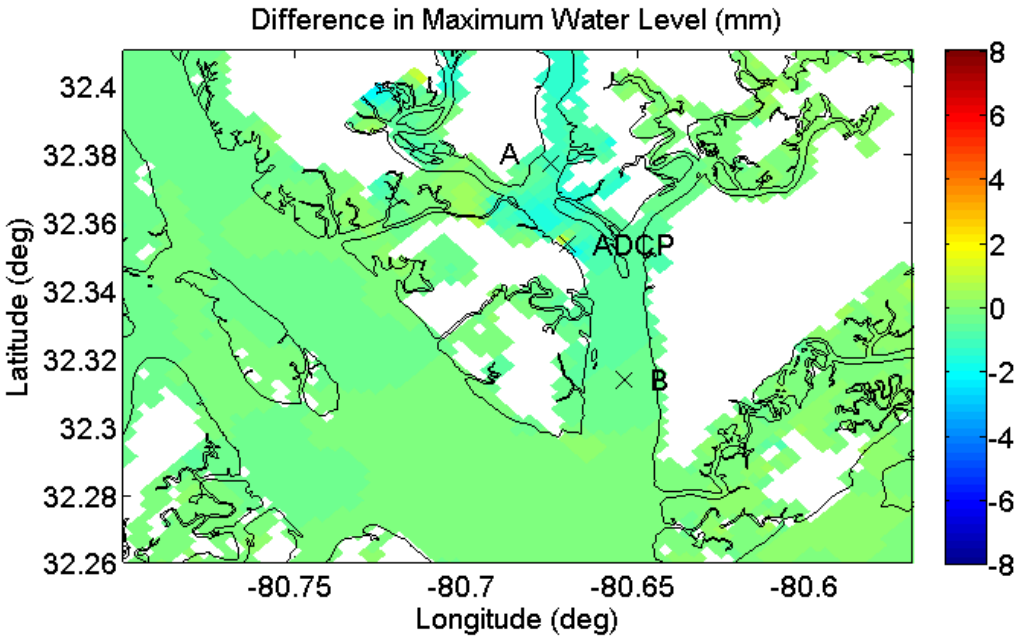

(a)

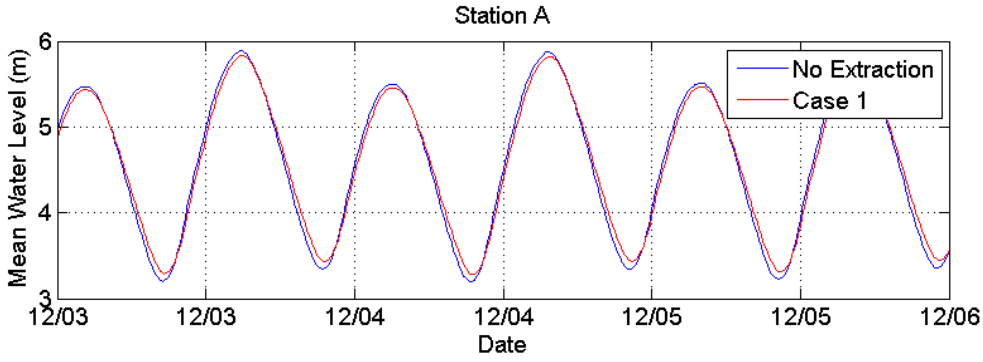

(b)

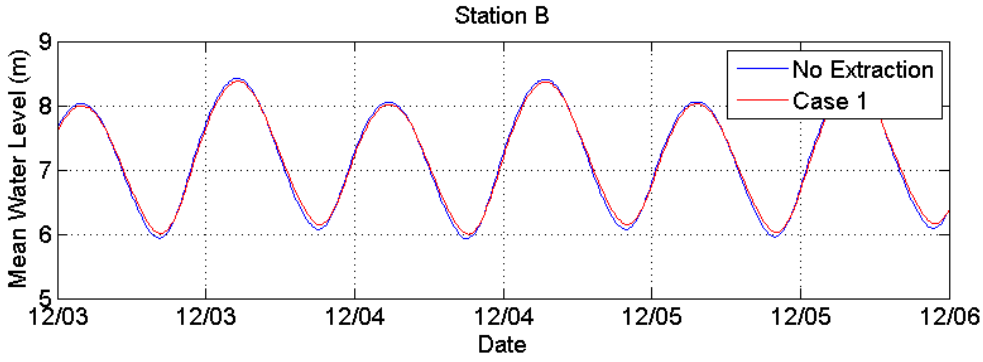

(c)

Figure 5.3. (a) Spatial difference in the maximum water surface elevation between the undisturbed flow case and the case with 10% kinetic energy extraction. Time series of mean water level at locations (b) upstream and (c) downstream of the extraction location.

Figure 5.4 shows time series of both the depth-averaged current speed and mean water level at the location of energy extraction (the ADCP Station), where the effects are the greatest in this case. The location of this point is indicated in Figures 5.2a and 5.3a. These time series are similar to those displayed previously in Figures 5.2 and 5.3. The same trends are observed at this location, with a more severe reduction in the current speed of about 0.4 m/s occurring during the maximum ebb tidal cycle. On average, the maximum depth-averaged flood and ebb current speeds are reduced by 0.11 m/s and 0.25 m/s in Case 1, respectively. This corresponds to a reduction in the depth-averaged flood and ebb current speeds by 16% and 29%, respectively. Again, there is little change in the mean water level at this location. A slight phase lag in current speed and mean water level is also observed. On average, the maximum flood and ebb current speeds occur 17.7 minutes later in Case 1.

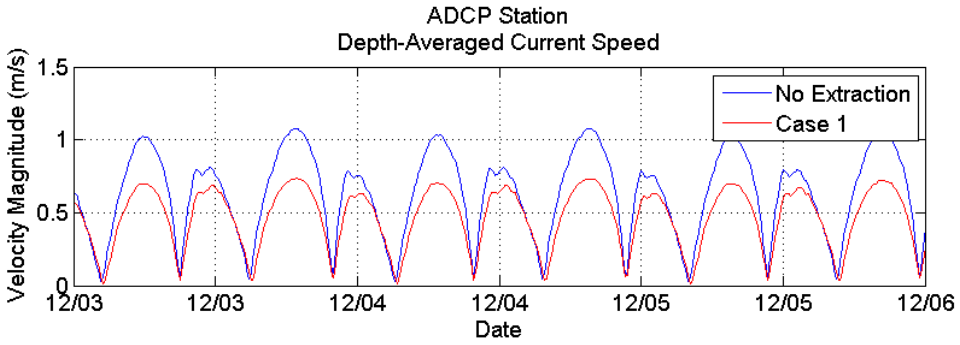

(a)

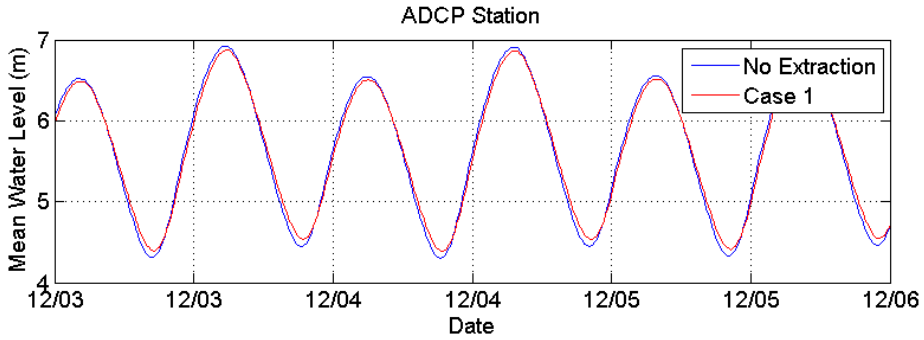

(b)

Figure 5.4. Time series of (a) the depth-averaged current speed and (b) the mean water level at the extraction location for the 10% kinetic energy extraction case.

A quantification of the differences in current speed and water level at the location of energy extraction is presented in Table 5.1. As in Chapter 4, a tidal decomposition was performed on both the current velocity and mean water level time series for the undisturbed flow case and Case 1. The Matlab toolbox "T-Tide" (Pawlowicz et al., 2002) was used to perform a harmonic analysis of both the modeled depth-averaged current velocity magnitude and mean water level time series. The results from this analysis are displayed for the four major constituents at this particular location for each of the four cases. As observed in Figure 5.4, both the water level and velocity amplitudes are reduced for each constituent in Case 1. In Table 5.1, the increased water level and velocity phase values in Case 1 indicated that there is a phase lag in the water level and current fluctuations. For instance, the water level fluctuations produced by the M2 tidal constituent for Case 1 lag those in the case with no energy extraction by 45.8 minutes. The velocity inclinations are also altered in Case 1 due to flow redirection around the extraction devices.

Table 5.1. Depth-averaged M2, N2, K1, and S2 tidal constituents and their properties derived from the ROMS model results for the no extraction case and the 10% kinetic energy extraction case at the extraction location. Velocity inclination corresponds to compass heading of major axis of tidal ellipse.

Constituent			M2	N2	K1	S2
Frequency	**hr^{-1}**	**No Extraction**	0.0805	0.0790	0.0418	0.0833
		Case 1	0.0805	0.0790	0.0418	0.0833
Water Level Amplitude	**m**	**No Extraction**	0.93	0.20	0.11	0.12
		Case 1	0.88	0.19	0.11	0.12
Water Level Phase	**degrees**	**No Extraction**	52.6	44.7	217.8	69.8
		Case 1	56.1	49.0	220.6	74.0
Velocity Amplitude	**m/s**	**No Extraction**	0.785	0.158	0.049	0.101
		Case 1	0.594	0.119	0.038	0.076
Velocity Phase	**degrees**	**No Extraction**	335.3	330.0	124.5	355.8
		Case 1	337.6	333.4	130.6	359.6
Velocity Inclination	**degrees**	**No Extraction**	129.8	129.3	130.0	129.3
		Case 1	129.1	129.4	129.5	129.4

The total amount of power dissipated from the channel cross-section due to the presence of the energy extraction devices in shown in Figure 5.5, along with the time series of the averaged current speeds across the channel before and after extraction. For Case 1, the amount of power dissipated reaches a maximum of 0.31 MW around December 4, 2009. The total power dissipated was found to be 62.8 MW-hrs per month which corresponds to 10.4% of the total 609.4 MW-hrs per month of kinetic energy throughout the cross-section in the undisturbed flow case. Note that for all four cases analyzed, the sum of the residual power and the power dissipated exceeds the amount of power contained in the original flow. This is due to the fact that the power dissipated includes both kinetic and potential energy losses, whereas, the original and residual power contained in the flow only account for kinetic energy. Furthermore, the total power dissipated includes the effects of energy losses due to turbulence and flow redevelopment. Therefore, the actual amount of energy generated by the extraction devices will be less than the total power dissipated, and will be further affected by the efficiency of the devices.

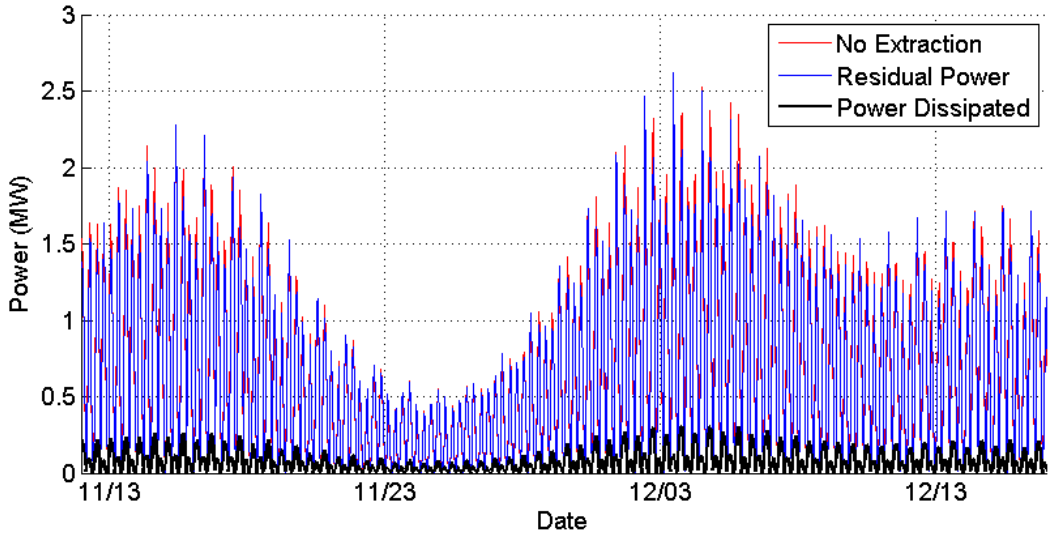

Figure 5.5. Time series of the tidal current power contained in the channel cross-section for the undisturbed flow case and the 10% kinetic energy extraction case, and the total power dissipated due to the energy extraction devices.

5.3 Case 2: 20% Kinetic Energy Extraction

Case 2 corresponds to the scenario in which 20% of the total kinetic energy contained in the channel cross-section at the extraction location is dissipated from the flow. For this case, an extraction coefficient of 0.01 was used in both the grid cell at the location of the longer-term ADCP deployment, and the adjacent cell in the cross-channel direction. Spatial changes in mean power density over the entire 35 day time span are shown in Figures 5.4. The maximum decrease in power density is observed immediately downstream of the grid cells containing the extraction devices, where the deficit in mean power density is about 23 W/m^2. It can be seen that the changes in mean power density are less pronounced than in Case 1, since the extraction is spread over two grid cells rather than one.

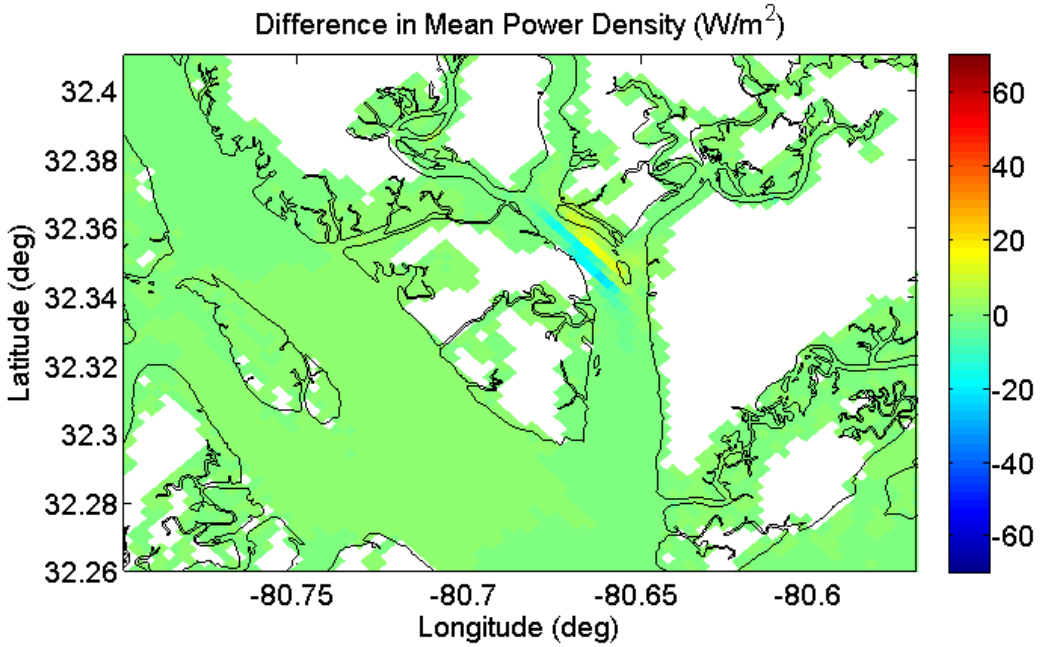

Figure 5.6. Spatial difference in mean power density between the undisturbed flow case and the case with 20% kinetic energy extraction.

The spatial variation in mean current speed follows the same trend as the changes in power density, and is presented in Figure 5.7a. Current speeds are reduced by less than 0.1 m/s near the extraction devices, and are again amplified throughout the

remainder of the channel cross-section. Again, these differences are less pronounced than in Case 1, because extraction is simulated over twice the surface area. In Figures 5.7b and 5.7c, there is little difference in the depth-averaged current speed time series at the upstream and downstream locations from those observed in Case 1. A slight reduction in the current speeds, similar to that in Case 1, is observed over the entire 3 day time span. The maximum difference in the peak depth-averaged current speeds at both stations is about 10 cm/s, which occurs during the ebb tidal cycle.

Figure 5.8a displays the difference in the maximum water level elevation between the undisturbed flow case and Case 2. In the immediate vicinity of the energy extraction location, an increase in the maximum water level is observed up to about 1 mm. This differs from Case 1, in which the water level in this area actually decreased. There is little difference in the mean water level time series in Figures 5.8b and 5.8c from Case 1. At each low tide, the water level is higher in Case 2, while at each high tide, the water level is lower in Case 2. A slight phase lag is also observed in Case 2.

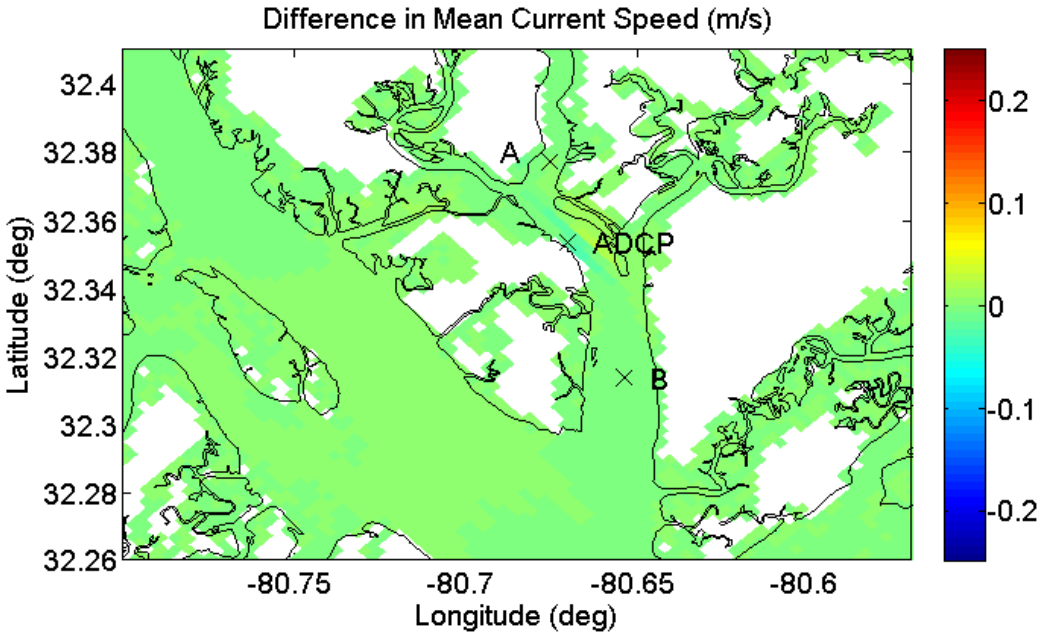

(a)

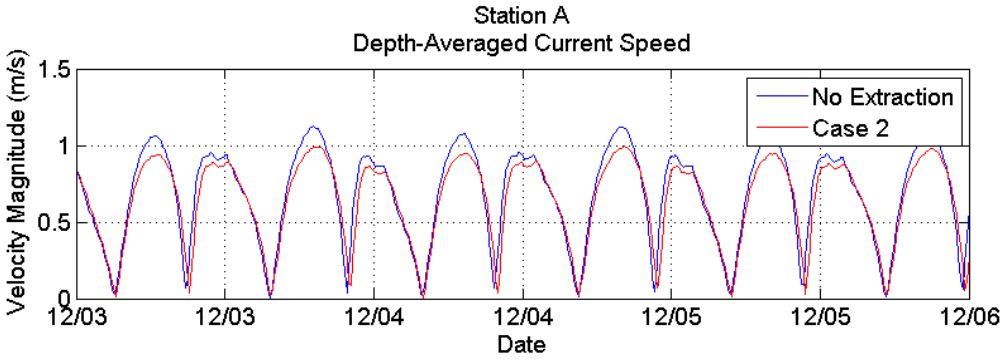

(b)

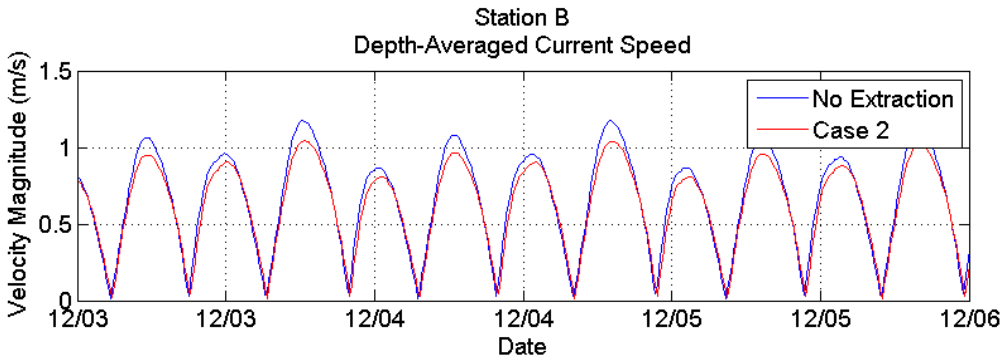

(c)

Figure 5.7. (a) Spatial difference in mean power density between the undisturbed flow case and the case with 20% kinetic energy extraction. Time series of depth-averaged current speed at locations (b) upstream and (c) downstream of the extraction location.

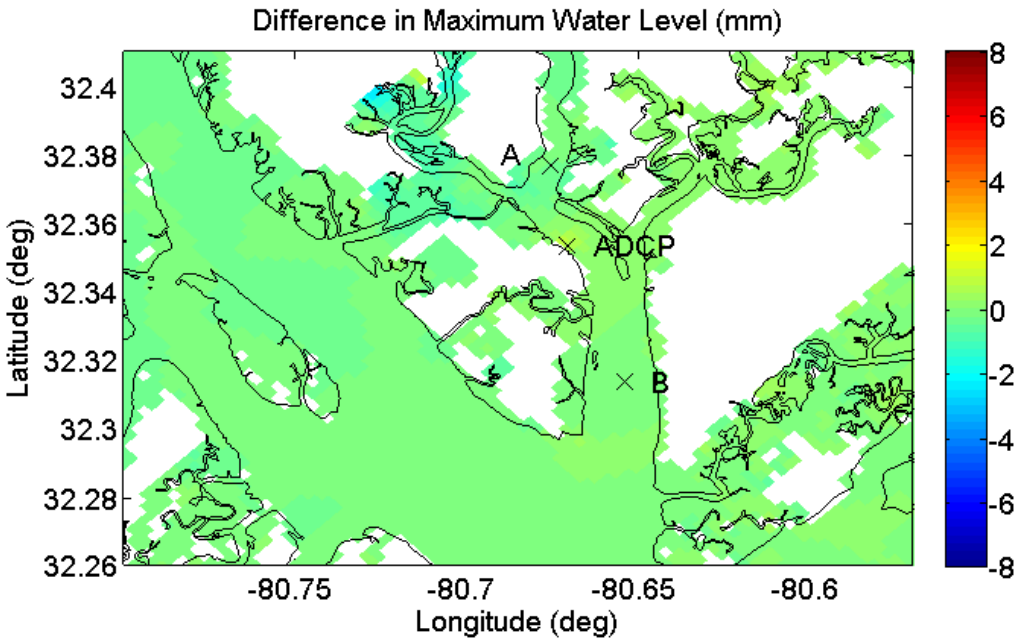

(a)

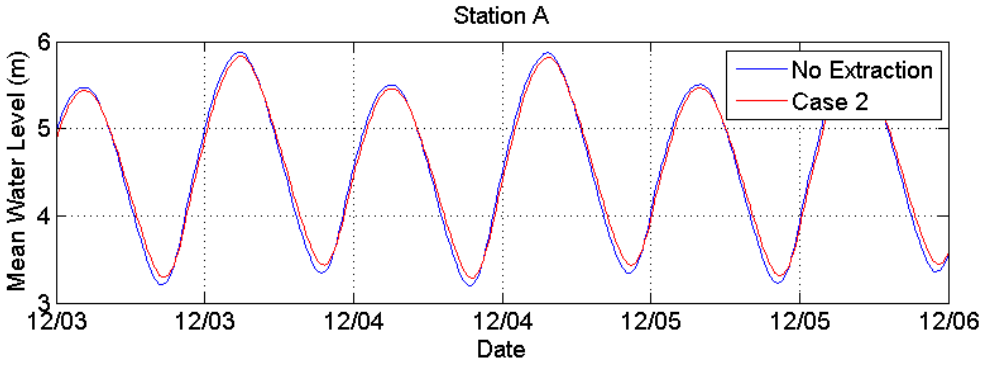

(b)

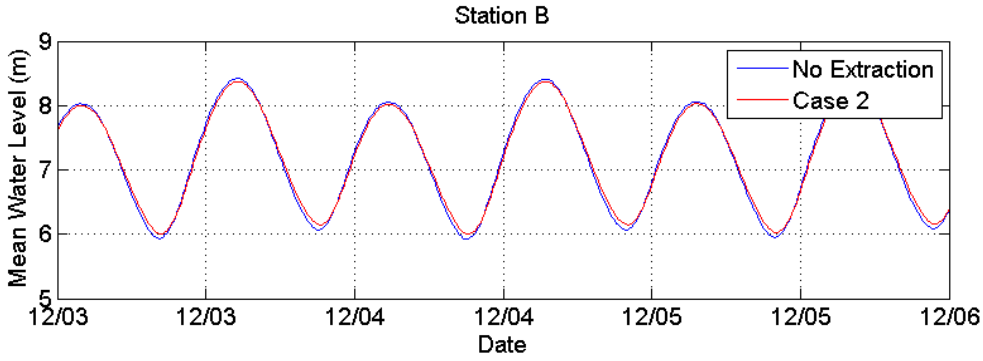

(c)

Figure 5.8. (a) Spatial difference in the maximum water surface elevation between the undisturbed flow case and the case with 20% kinetic energy extraction. Time series of mean water level at locations (b) upstream and (c) downstream of the extraction location.

Figure 5.9 shows time series of both the depth-averaged current speed and mean water level at the location of energy extraction. In Case 2, there is a smaller reduction in the current speeds than in Case 1, since the extraction is spread over two grid cells. The maximum deficit in current speed at this location is about 0.2 m/s for this case. The maximum flood current speeds are reduced by 0.04 m/s (6%) while the maximum ebb current speeds are reduced by 0.12 m/s (14%). The maximum currents in Case 2 occur 17.5 minutes later, on average. There is little change in the mean water level time series, and slight phase difference in current speed and mean water level is observed.

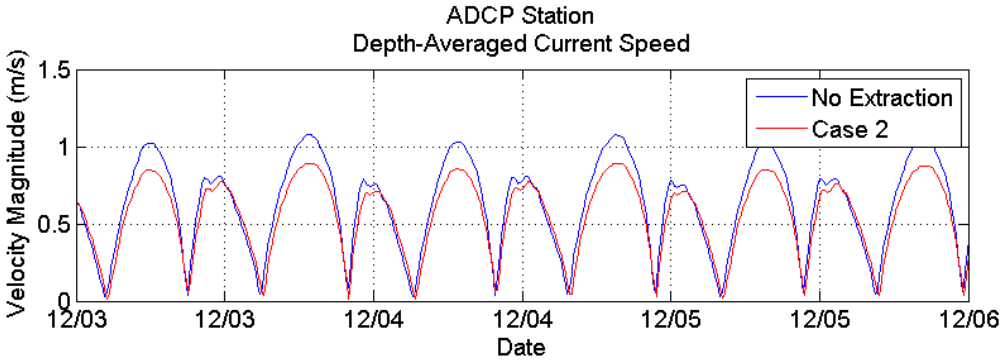

(a)

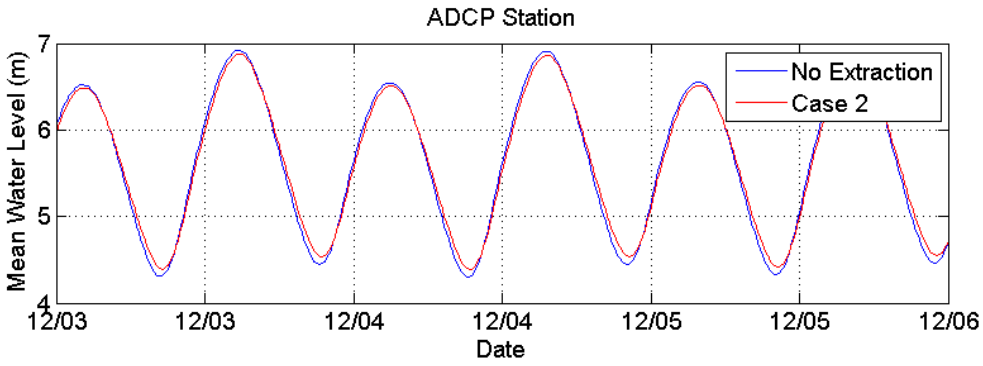

(b)

Figure 5.9. Time series of (a) the depth-averaged current speed and (b) the mean water level at the extraction location for the 20% kinetic energy extraction case.

In Case 2, both the water level and velocity amplitude of each of the four major tidal constituents at the extraction location shown in Table 5.2 are lower than the undisturbed case. The water level and velocity phase for each constituent lags that of the no extraction case. The water level fluctuations produced by the M2 tidal constituent occur 45.8 minutes later in Case 2. This phase lag is identical to that observed in Case 1. Again, the velocity inclinations are altered slightly in Case 2 due to flow redirection around the extraction devices.

Table 5.2. Depth-averaged M2, N2, K1, and S2 tidal constituents and their properties derived from the ROMS model results for the no extraction case and the 20% kinetic energy extraction case at the extraction location. Velocity inclination corresponds to compass heading of major axis of tidal ellipse.

Constituent			M2	N2	K1	S2
Frequency	**hr^{-1}**	**No Extraction**	0.0805	0.0790	0.0418	0.0833
		Case 2	0.0805	0.0790	0.0418	0.0833
Water Level Amplitude	**m**	**No Extraction**	0.93	0.20	0.11	0.12
		Case 2	0.88	0.19	0.11	0.12
Water Level Phase	**degrees**	**No Extraction**	52.6	44.7	217.8	69.8
		Case 2	56.1	49.1	220.7	74.1
Velocity Amplitude	**m/s**	**No Extraction**	0.785	0.158	0.049	0.101
		Case 2	0.705	0.140	0.045	0.090
Velocity Phase	**degrees**	**No Extraction**	335.3	330.0	124.5	355.8
		Case 2	338.2	334.2	129.6	359.8
Velocity Inclination	**degrees**	**No Extraction**	129.8	129.3	130.0	129.3
		Case 2	130.6	130.4	130.7	130.4

Figure 5.10 shows the the time series of the total amount of power dissipated from the channel cross-section due to the presence of the energy extraction devices, along with the available and residual power across the channel. The amount of power dissipated reaches a maximum of 0.53 MW for this case. The total power dissipated per month was found to be 117.1 MW-hrs per month which corresponds to 19.4% of the total 609.4

MW-hrs per month of kinetic energy throughout the cross-section in the undisturbed flow case.

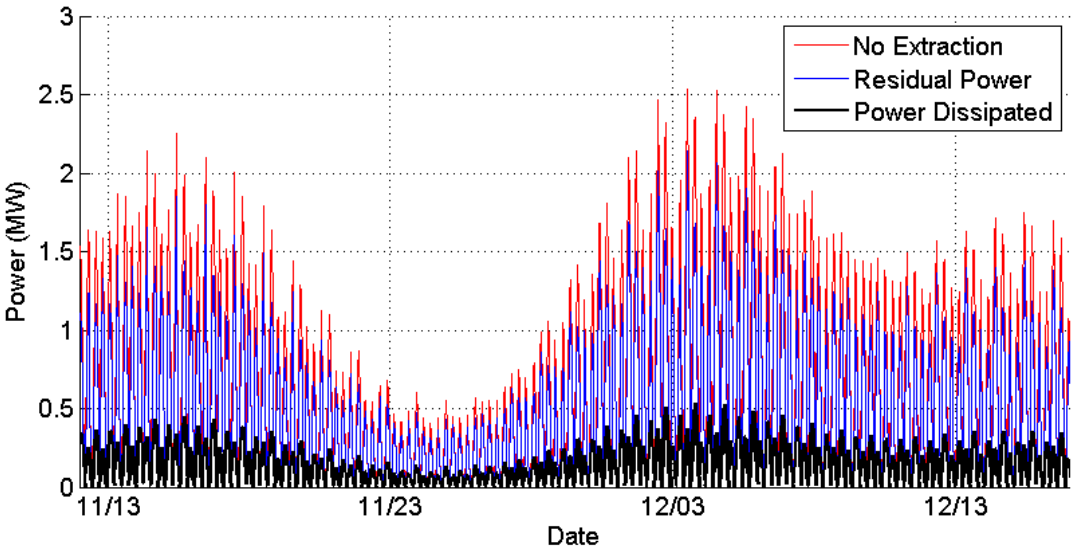

Figure 5.10. Time series of the tidal current power contained in the channel cross-section for the undisturbed flow case and the 20% kinetic energy extraction case, and the total power dissipated due to the energy extraction devices.

5.4 Case 3: 30% Kinetic Energy Extraction

Case 3 corresponds to the scenario in which approximately 30% of the total kinetic energy contained in the channel cross-section at the extraction location is dissipated from the flow. The extraction was simulated in two grid cells, similar to Case 2. In this case, however, the extraction coefficient was increased to 0.018 in the ADCP grid cell and the adjacent cell in the cross-channel direction. In Figure 5.11, it can be seen that the decrease in mean power density is greatest just downstream from the extraction location. The power density increases throughout the remainder of the channel, similar to the previous two cases. A maximum deficit in power density of about 40 W/m^2 and a maximum increase in power density of about 30 W/m^2 are observed in these locations.

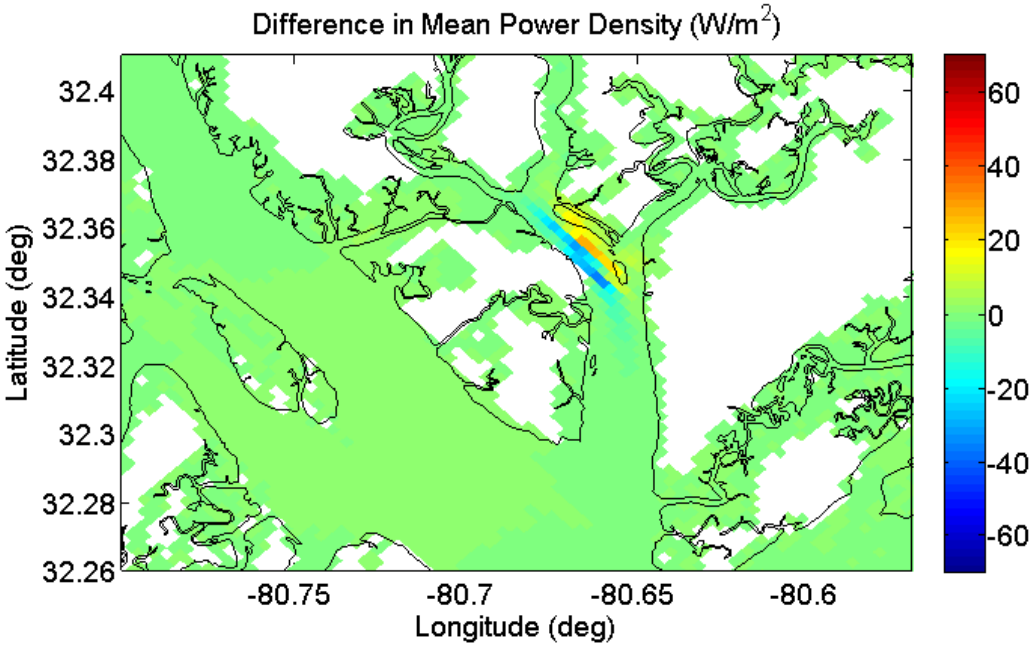

Figure 5.11. Spatial difference in mean power density between the undisturbed flow case and the case with 30% kinetic energy extraction.

The spatial difference in mean current speed for the entire 35 day model time span, shown in Figure 5.12a, follows a similar pattern to that observe in the spatial power density plot in Figure 5.11. The deficit in mean current speed is approximately 5 cm/s just downstream from the extraction location. There is little change in the time series of depth-averaged current speed at Stations A and B in this case from those displayed in Case 2. Differences in the maximum water level elevation observed over the 35 day time span are minimal in this case, as in the two previous cases, and are shown in Figure 5.13a. A maximum drop in water level of merely 4 mm is observed upstream from the extraction location. The water level seems to increase by no more than 2 mm on the downstream side of the extraction devices. As with the depth-averaged current time series, there are minimal differences in the mean water level time series upstream and downstream from the ADCP station from those seen in Case 2.

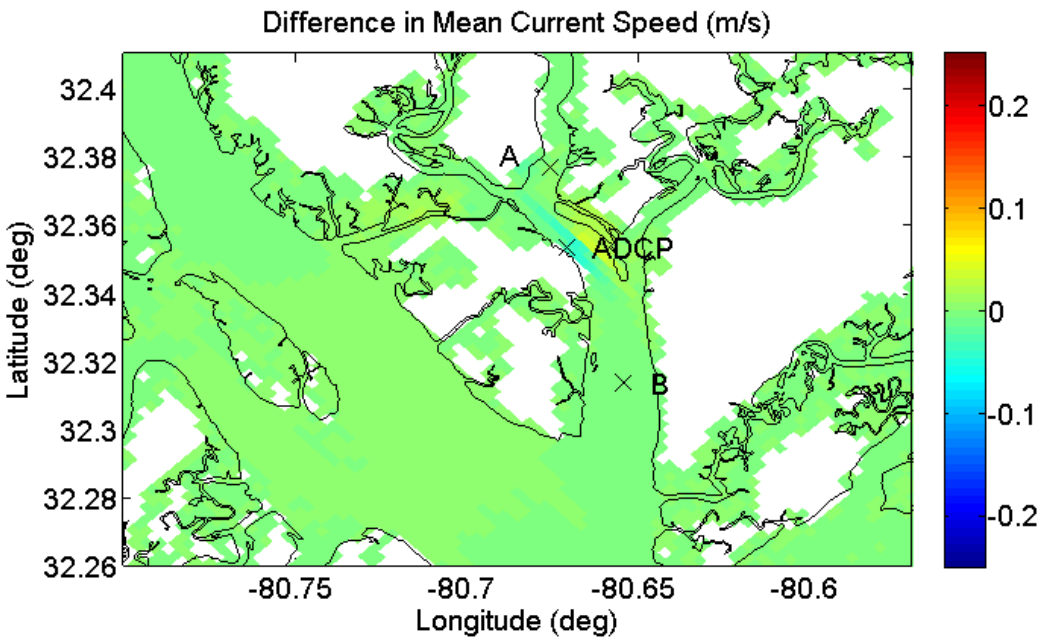

(a)

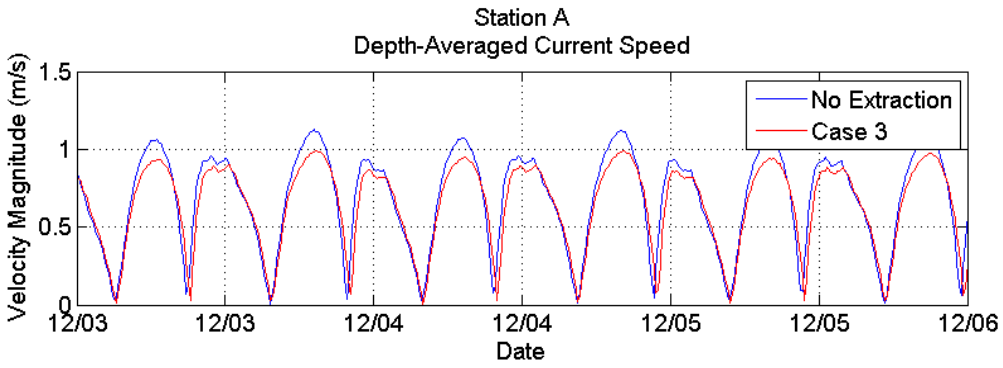

(b)

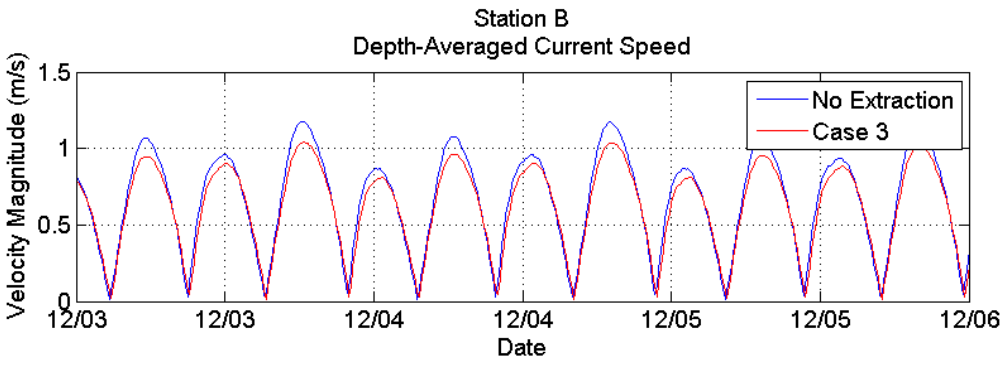

(c)

Figure 5.12. (a) Spatial difference in mean power density between the undisturbed flow case and the case with 30% kinetic energy extraction. Time series of depth-averaged current speed at locations (b) upstream and (c) downstream of the extraction location.

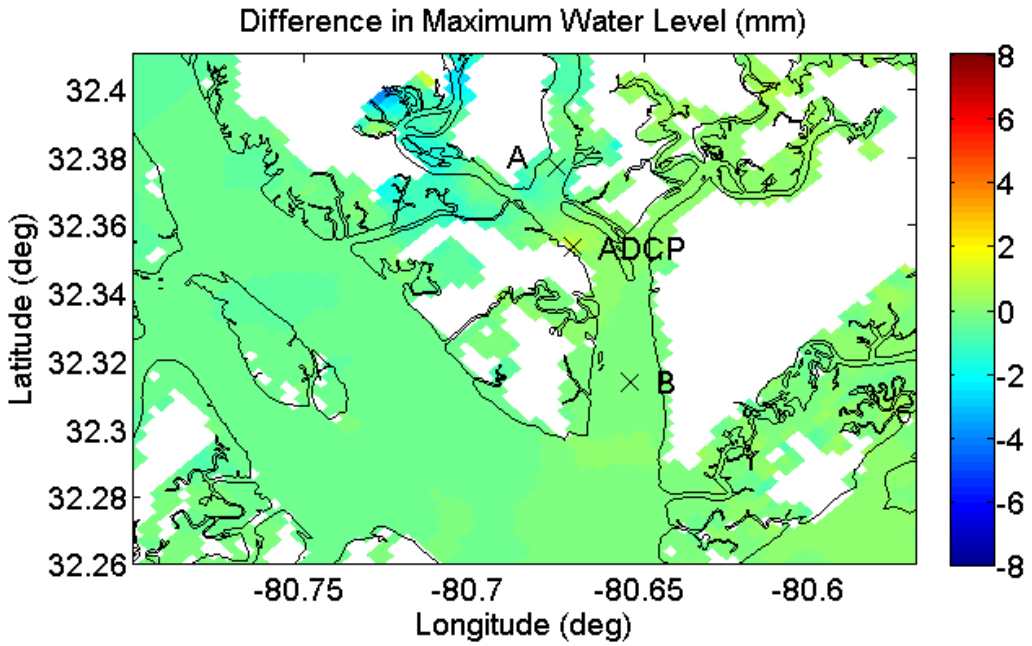

(a)

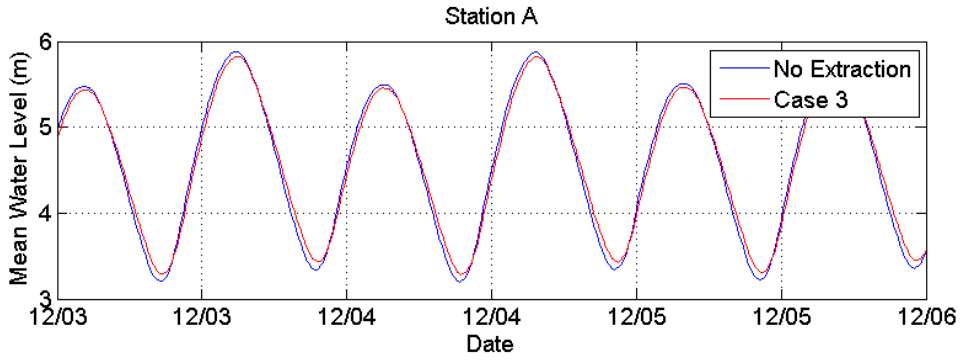

(b)

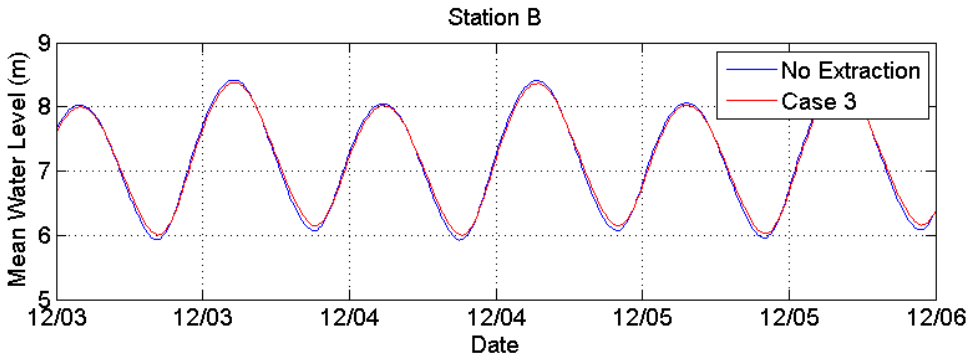

(c)

Figure 5.13. (a) Spatial difference in the maximum water surface elevation between the undisturbed flow case and the case with 20% kinetic energy extraction. Time series of mean water level at locations (b) upstream and (c) downstream of the extraction location.

Differences in depth-averaged currents are more evident at the extraction location and are displayed below in Figure 5.14a. The difference is greatest during the ebb tidal cycle, where a maximum deficit of about 0.25 m/s is observed. This deficit is greater than that observed in Case 2, because the extraction coefficient has been increased in this case. On average, the maximum flood and ebb current speeds are reduced by 0.05 m/s (7%) and 0.15 m/s (17%), respectively. These maximum current speeds occur 17.4 minutes later in this case. The mean water level time series is nearly identical to the previous case.

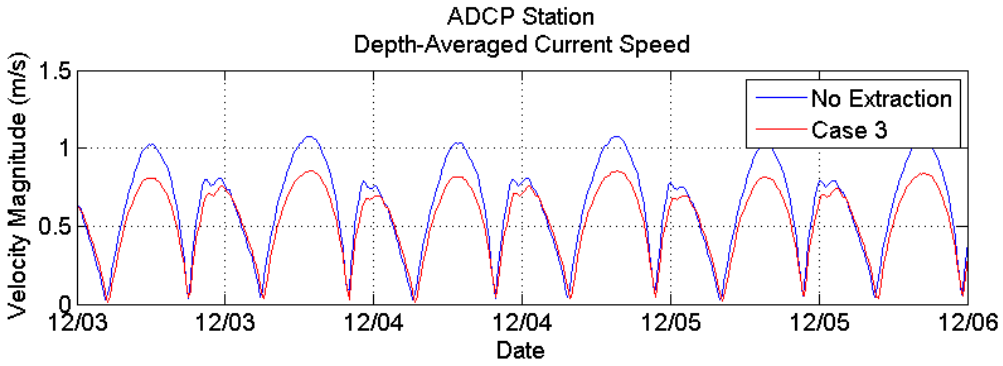

(a)

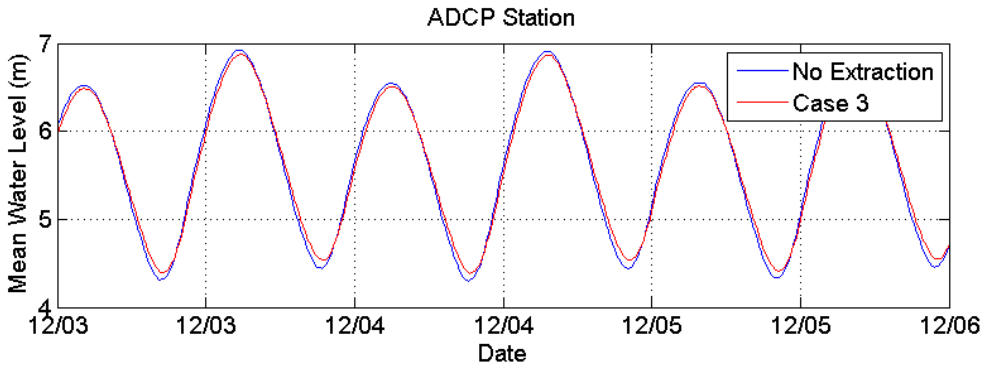

(b)

Figure 5.14. Time series of (a) the depth-averaged current speed and (b) the mean water level at the extraction location for the 30% kinetic energy extraction case.

In Table 5.3, it can be seen that the changes in the water level constituent phases are minimal when compared to those computed for Case 2, while the water level

amplitude changes are identical. The velocity amplitude for each of the four major constituents is slightly lower in Case 3 than in the previous case. A phase shift in both the water level and velocity constituents is evident, although minimal. Water level fluctuations caused by the M2 tidal constituent lag the case with no extraction by 46.8 minutes.

Table 5.3. Depth-averaged M2, N2, K1, and S2 tidal constituents and their properties derived from the ROMS model results for the no extraction case and the 30% kinetic energy extraction case at the extraction location. Velocity inclination corresponds to compass heading of major axis of tidal ellipse.

Constituent			M2	N2	K1	S2
Frequency	**hr^{-1}**	**No Extraction**	0.0805	0.0790	0.0418	0.0833
		Case 3	0.0805	0.0790	0.0418	0.0833
Water Level Amplitude	**m**	**No Extraction**	0.93	0.20	0.11	0.12
		Case 3	0.88	0.19	0.11	0.12
Water Level Phase	**degrees**	**No Extraction**	52.6	44.7	217.8	69.8
		Case 3	56.2	49.1	220.7	74.1
Velocity Amplitude	**m/s**	**No Extraction**	0.785	0.158	0.049	0.101
		Case 3	0.682	0.140	0.043	0.087
Velocity Phase	**degrees**	**No Extraction**	335.3	330.0	124.5	355.8
		Case 3	337.6	333.9	129.5	359.5
Velocity Inclination	**degrees**	**No Extraction**	129.8	129.3	130.0	129.3
		Case 3	131.0	130.9	131.2	130.9

The maximum amount of power dissipated from the flow in Case 3 was calculated to be 0.85 MW, as shown in Figure 5.15. The total power dissipated by the extraction devices in a one month time period was found to be 189.4 MW-hrs per month, which corresponds to 31.3% of the available 609.4 MW-hrs per month of kinetic energy in the undisturbed flow. The residual power time series for this case is nearly identical to that of Case 2, although in this case an additional 72.3 MW-hrs per month is dissipated from the flow.

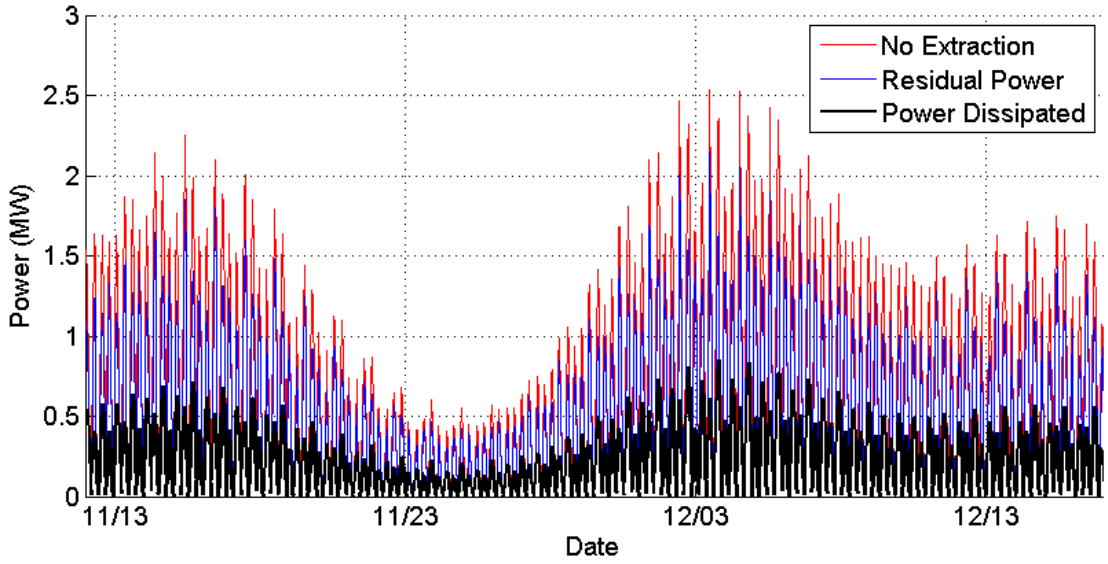

Figure 5.15. Time series of the tidal current power contained in the channel cross-section for the undisturbed flow case and the 30% kinetic energy extraction case, and the total power dissipated due to the energy extraction devices.

5.5 Case 4: 60% Kinetic Energy Extraction

Case 4 represents a proposed theoretical extreme in which 60% of the total kinetic energy contained in the channel cross-section at the extraction location is dissipated from the flow. This is modeled in a similar fashion to cases 2 and 3, with the coefficient of extraction raised to 0.05 in two grid cells. Figure 5.9 displays the effect of energy extraction on the mean current speed and mean power density. Similar patterns seen previously in cases 2 and 3 are observed for this case, but the deviations from the undisturbed case are more severe. Differences in power density are shown in Figure 5.16, and follow the same general trends as in the previous cases with a maximum deficit of about 70 W/m^2 downstream of the extraction area and a maximum increase of about 70 W/m^2 in the remainder of the channel.

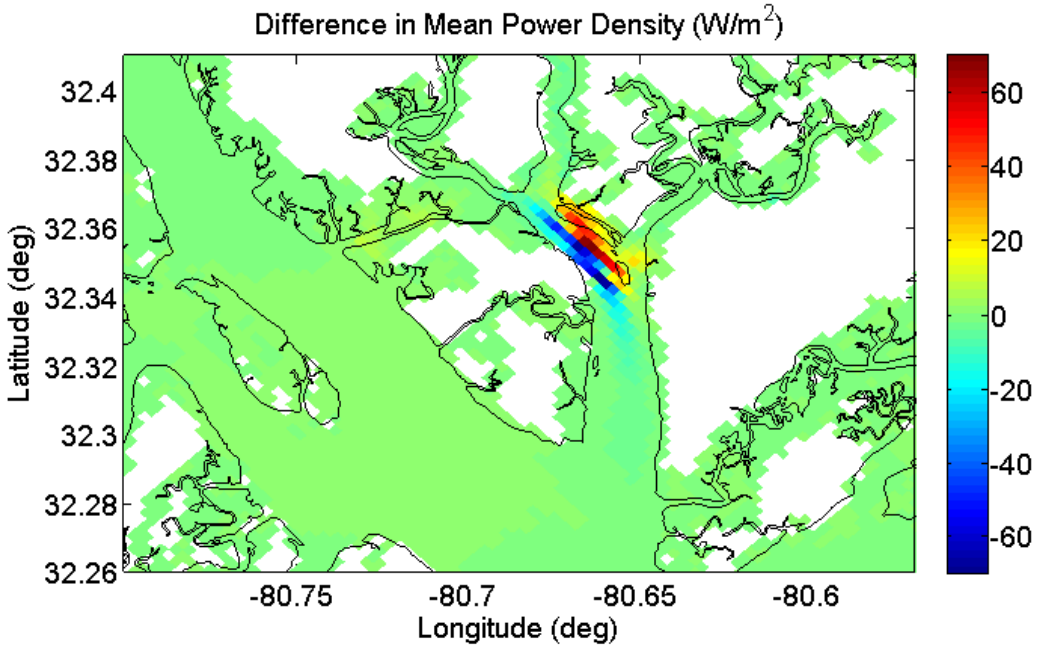

Figure 5.16. Spatial difference in mean power density between the undisturbed flow case and the case with 60% kinetic energy extraction.

In Figure 5.17a, current speeds are reduced by approximately 0.1 m/s in the grid cells containing the extraction devices, and are amplified by about 0.1 m/s throughout the rest of the channel cross-section. A slight increase in current speed is also observed in the narrow channel connecting the Broad and Beaufort Rivers on the north side of Parris Island. Minimal differences from Cases 2 and 3 are present in the depth-averaged current velocity time series both upstream and downstream from the extraction location.

Differences in the maximum water surface elevation are also amplified in Case 4 and are displayed in Figure 5.10a. The water surface elevation increases downstream of the extraction area and decreases upstream, with a maximum deviation of 8 mm upstream. Again, the time series for mean water level are nearly identical to the previous two cases. Overall, the changes in water level due to the removal of energy from the system are trivial, even in the extreme case in this study.

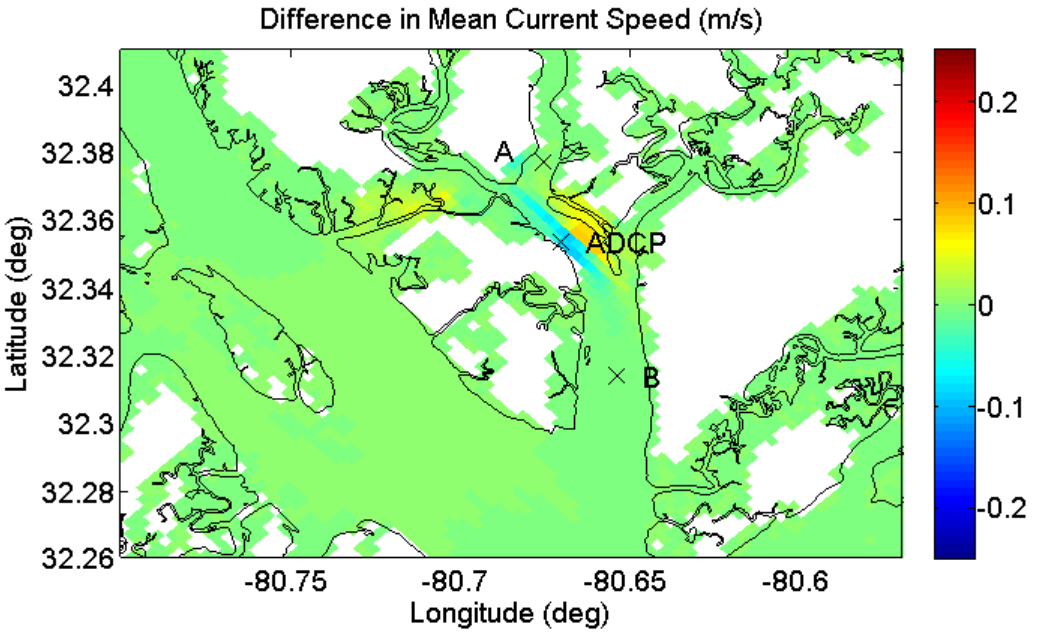

(a)

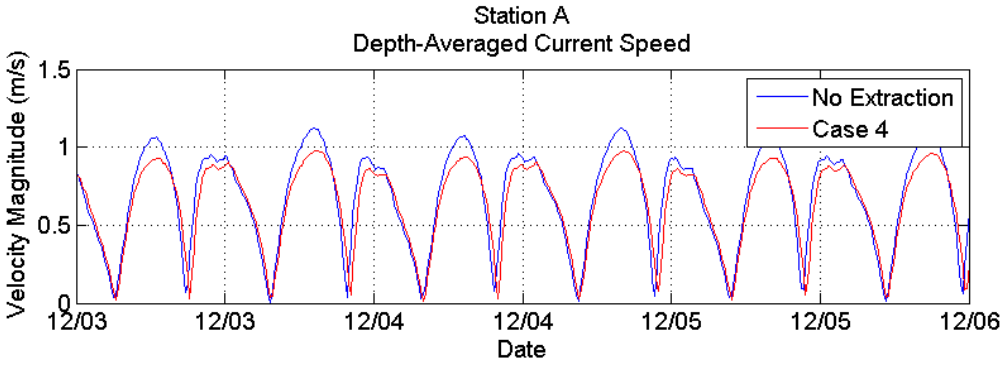

(b)

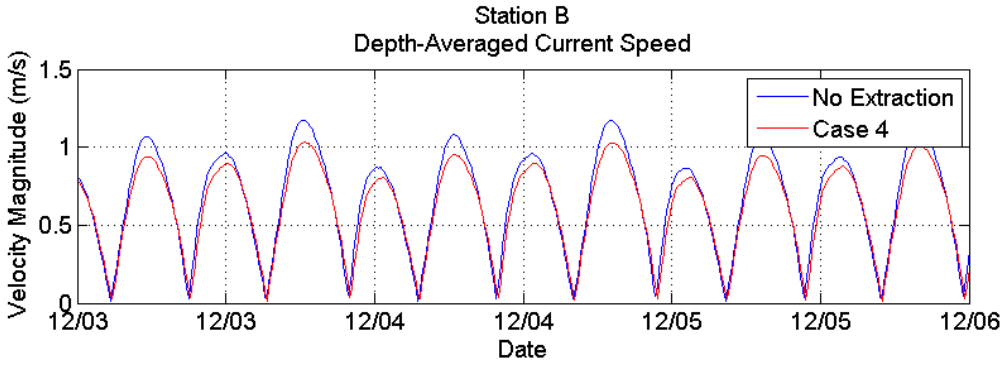

(c)

Figure 5.17. (a) Spatial difference in mean power density between the undisturbed flow case and the case with 60% kinetic energy extraction. Time series of depth-averaged current speed at locations (b) upstream and (c) downstream of the extraction location.

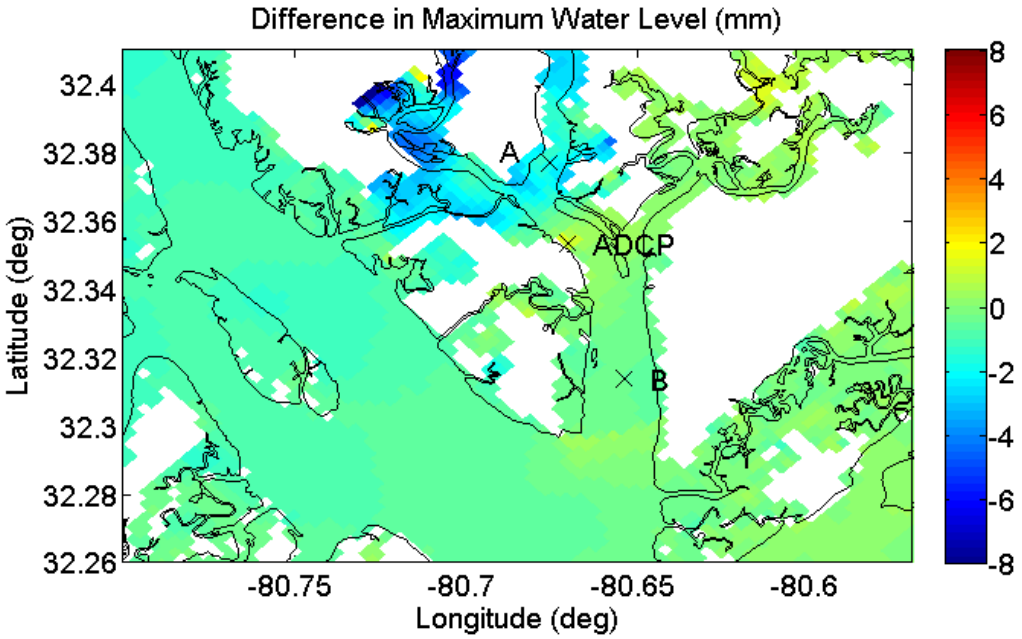

(a)

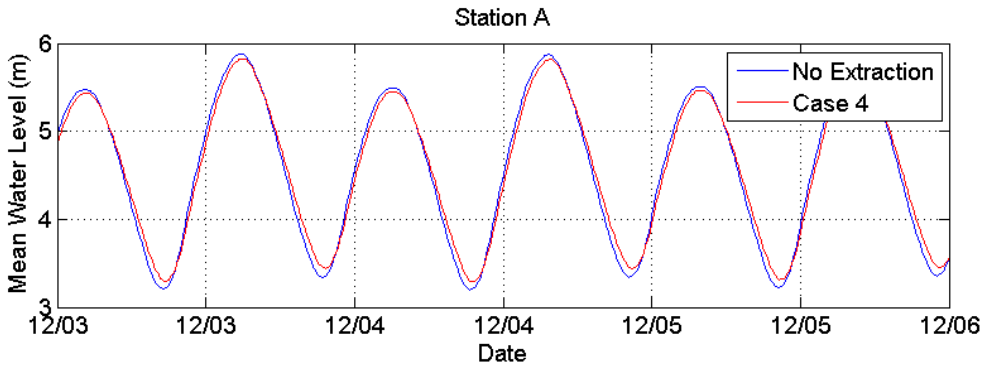

(b)

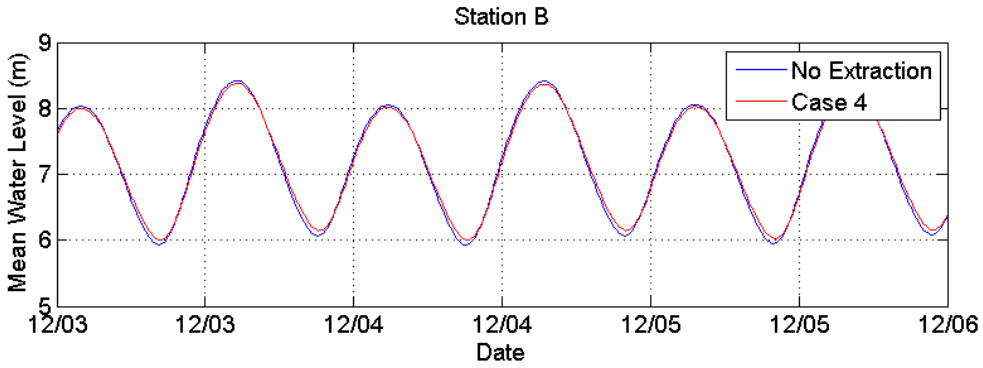

(c)

Figure 5.18. (a) Spatial difference in the maximum water surface elevation between the undisturbed flow case and the case with 60% kinetic energy extraction. Time series of mean water level at locations (b) upstream and (c) downstream of the extraction location.

The depth-averaged current speeds in Case 4 are further reduced from the previous cases due to the increased extraction coefficient. The time series in Figure 5.19a is now nearly identical to that shown previously for Case 1, where 10% of the total energy was dissipated from a single grid cell. In this case, the maximum flood current speeds are reduced by 0.1 m/s (14%) while the maximum ebb current speeds are reduced by 0.25 m/s (29%), on average. These maximum currents occur 17.5 minutes later in Case 4. The mean water level time series in Figure 5.19b shows little change at this location when compared to previous cases.

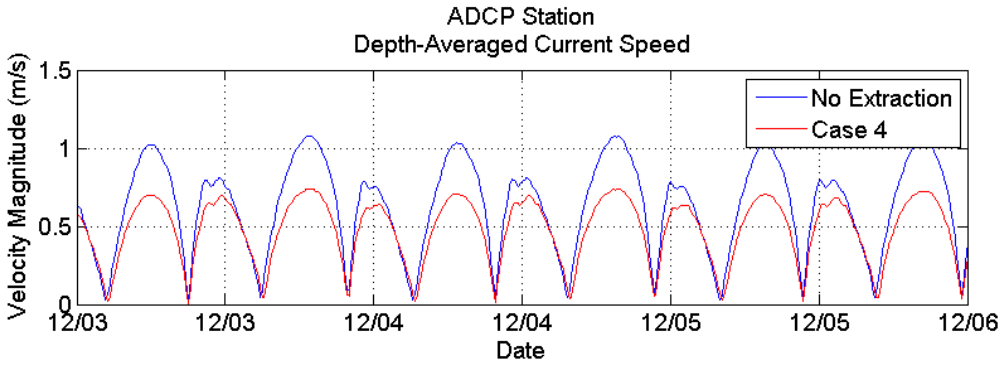

(a)

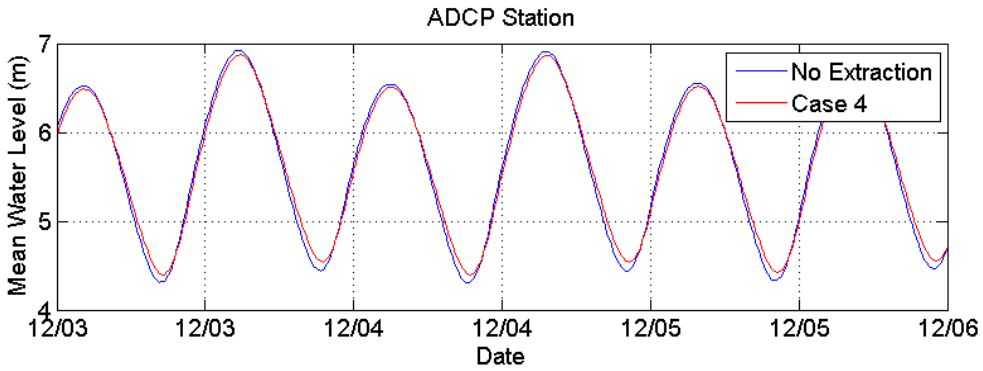

(b)

Figure 5.19. Time series of (a) the depth-averaged current speed and (b) the mean water level at the extraction location for the 60% kinetic energy extraction case.

In Table 5.4, the water level amplitude for the four major tidal constituents at the extraction location is identical to the two previous cases. However, the current velocity

amplitude continues a decreasing trend for each constituent from the two previous cases. Both the velocity and water level changes are lagging the undisturbed case, as evidenced by the increase in phase values, but differ marginally from the previous cases. The water level fluctuations caused by the M2 tidal constituent occur 46.8 minutes later in Case 4. This phase shift is identical to that observed in the previous case.

Table 5.4. Depth-averaged M2, N2, K1, and S2 tidal constituents and their properties derived from the ROMS model results for the no extraction case and the 60% kinetic energy extraction case at the extraction location. Velocity inclination corresponds to compass heading of major axis of tidal ellipse.

Constituent			M2	N2	K1	S2
Frequency	**hr^{-1}**	**No Extraction**	0.0805	0.0790	0.0418	0.0833
		Case 4	0.0805	0.0790	0.0418	0.0833
Water Level Amplitude	**m**	**No Extraction**	0.93	0.20	0.11	0.12
		Case 4	0.88	0.19	0.11	0.12
Water Level Phase	**degrees**	**No Extraction**	52.6	44.7	217.8	69.8
		Case 4	56.2	49.2	220.7	74.1
Velocity Amplitude	**m/s**	**No Extraction**	0.785	0.158	0.049	0.101
		Case 4	0.610	0.121	0.039	0.077
Velocity Phase	**degrees**	**No Extraction**	335.3	330.0	124.5	355.8
		Case 4	336.5	333.4	129.6	359.0
Velocity Inclination	**degrees**	**No Extraction**	129.8	129.3	130.0	129.3
		Case 4	131.7	131.8	132.1	131.8

The maximum power dissipated from the flow, displayed in Figure 5.20, is increased dramatically compared to the previous three cases. In Case 4, the maximum power dissipated reaches 1.59 MW, nearly twice that calculated for Case 3. A total of 370.8 MW-hrs per month of power is dissipated from the flow, accounting for 61.4% of the 609.4 MW-hrs per month of kinetic energy contained in the original flow. Still, there is little effect on the average residual power across the channel cross-section at this location.

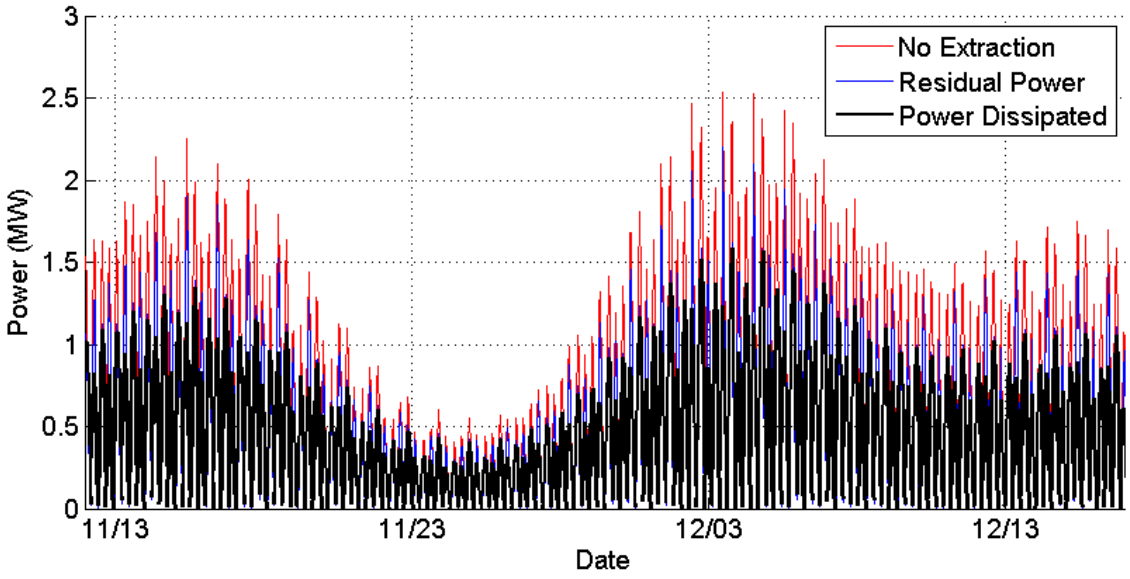

Figure 5.20. Time series of the tidal current power contained in the channel cross-section for the undisturbed flow case and the 60% kinetic energy extraction case, and the total power dissipated due to the energy extraction devices.

5.6 Summary

In each of the 4 cases considered in this study, both the tidal current velocities and mean water level in the vicinity of Parris Island are affected by the extraction of power from the flow. Upstream from the extraction location, the mean water level is lower in each case. Both the water level and current velocity phases are also affected by the dissipation of power in each case. The maximum flood and ebb currents occur 17 to 18 minutes later in each case, compared to the case with no energy extraction. Current velocities immediately upstream and downstream from the simulated extraction devices are reduced in each case, while being amplified throughout the portion of the channel cross-section without extraction. On the downstream side of the extraction location, a greater reduction in current speeds, and thus power density, is observed. This occurs because current speeds during the ebb tidal cycles tend to be greater than during the flood tidal cycles at this location; therefore, there is more available energy during the ebb tidal cycles, resulting in the dissipation of a greater amount of energy at these times. These

changes, however, are minimal even in the extreme case in which 61.4% of the total kinetic energy in the channel cross-section at the extraction location is dissipated by the devices. In each case, moderate impacts are observed at the extraction location, however, upstream and downstream of this area, the impacts are relatively insignificant. When extraction is spread out over a larger surface area, as in Cases 2, 3, and 4, the power generation potential is increased greatly with minor additional impacts at the extraction location.

CHAPTER 6

CONCLUSIONS

To combat the global dependence on fossil fuels as the primary source of energy, research must be conducted to develop methods for utilizing various types of renewable energy that have minimal negative environmental impacts. The energy of the tides represents one of these types of renewable energy, and has the potential to play a major role in a sustainable future. This energy can be harnessed using extraction devices such as marine current turbines and tidal barrages. In order to evaluate the potential of a particular location to produce significant amounts of energy using these types of devices, extensive investigations must be conducted to determine important site characteristics such as water depth, current velocity, and water level fluctuations over time. The periodicity and predictability of the tides are one of the key advantages of this globally existent energy resource, which allow for accurate predictions of key site properties.

The Marine Corps Recruit Depot located on Parris Island, South Carolina, is situated between the confluence of the Broad and Beaufort Rivers. These are tidally dominated rivers, which experience some of the largest tidal ranges in the southeastern United States, between 2.5 and 3 meters during "spring" tide periods. An assessment of the potential for tidal energy extraction using marine current turbines at a particular location in the Beaufort River near Parris Island is presented in this thesis. Because Parris Island already has much of the necessary land-based infrastructure in place, there is logical potential for the extraction of kinetic energy from the nearby tidal streams using underwater turbines for power production. This potential was evaluated using in-situ measurements in the vicinity of the pump station on Parris Island and the Regional Ocean Modeling System (ROMS). The potential impacts on the hydrodynamics in this area were also evaluated using the ROMS model.

Results from in-situ measurements indicate that tidal currents along the portion of the Beaufort River analyzed in this study are driven primarily by the semi-diurnal M2 tidal constituent. The tidal range at the study site is approximately 2 meters on average, with a mean depth-averaged current velocity magnitude of 0.57 m/s predicted for a period of one year. A mean depth-averaged current velocity magnitude of 0.59 m/s was observed over the course of the longer-term acoustic Doppler current profiler (ADCP) deployment from November 12 to December 17, 2009. The physical characteristics of the site and its proximity to the energy plant on Parris Island are favorable attributes for tidal energy extraction. The maximum current speed at the site is approximately 1.2 m/s at the water surface. Due to the relatively shallow water depth and moderate velocities at this location, the generation of modest amounts of energy is possible with the utilization of low-flow, possibly floating, turbines. For example, with a 10 m^2 intake area, a turbine with 50% efficiency would generate 8400 kW-hrs of energy per year.

In addition to the in-situ measurements, the tidal currents in the vicinity of Parris Island, SC were assessed using ROMS. The model was run to match the dates of the in-situ ADCP deployment and was calibrated using measurements from the instrument during that time period. Results from the model allowed for a better spatial observation of the currents in the Beaufort River in the vicinity of the study area. The ROMS model applied to the coastal areas surrounding Parris Island, SC produces results that closely resemble in-situ measurements collected previously during both the boat-based survey and the longer-term ADCP deployment. Although the modeled water level phase differs from the measurements by 13.8 minutes on average, the modeled current velocities, which are of more importance, are highly accurate. Maximum current velocities predicted by the model are 94.5% of those observed in the field. Furthermore, spatial variations in current speed and power density agree well with in-situ measurements. Therefore, this version of the model was used to simulate the effects of the placement of underwater turbines on the local hydrodynamics.

In the analysis of the effects of energy extraction from the system, four separate cases were considered in which 10, 20, 30, and 60% of the total kinetic energy contained in the flow was dissipated near the location of the longer-term ADCP deployment. The effect of power extraction from the tidal flow is simulated by introducing an additional sink term into the governing momentum equations in the grid cells containing the extraction devices. In each of the 4 cases considered in this study, both the tidal current velocities and mean water level in the vicinity of Parris Island are affected by the extraction of power from the flow. Upstream from the extraction location, the mean water level is lower in each case. Current velocities immediately upstream and downstream from the simulated extraction devices are reduced in each case, while being amplified throughout the portion of the channel cross-section without extraction. These changes, however, are minimal even in the extreme case in which 61.4% of the total kinetic energy in the channel cross-section at the extraction location is dissipated by the devices. When extraction is spread out over a larger surface area, as in Cases 2, 3, and 4, the power generation potential is increased greatly with minor additional negative impacts on the surrounding flow field.

The impacts of energy extraction at the site analyzed in this study were found to be negligible for two primary reasons. First, the maximum current speed of 1.2 m/s observed at the extraction location is considered to be moderate in comparison to other locations that have been considered for power extraction. Therefore, a limited amount of energy is dissipated from the flow field, contributing to the minimal far-field effects observed in the presence of extraction in each of the four cases considered. Second, although over 60% of the total kinetic energy contained in the flow is dissipated in Case 4, the simulated extraction takes place over less than half of the overall channel cross-section. Since over half of the channel cross-section is unobstructed by the presence of energy extraction devices, there is ample space for a portion of the flow to bypass the

extraction location. This leads to better flow recovery and minimal impacts on the local water level and currents.

The data presented in this thesis is intended to be a preliminary investigation of the tidal stream energy potential at Parris Island. Prior to implementing the use of marine current turbines in harnessing tidal energy at this location, a much more extensive assessment of the site characteristics must be completed. For instance, a much more detailed assessment of the current velocity profile throughout the study site in which turbulence, eddies, and other complex variations in the flow are observed and quantified. This can be accomplished through the deployment of numerous ADCP's and acoustic Doppler velocimeters (ADV's) throughout the area of interest. These types of flow characteristics are significant since they can greatly affect the performance of submerged energy extraction devices, and the external loading applied to them by the flow. Furthermore, the bottom sediment characteristics must be determined and considered when selecting a type of extraction device and the anchoring mechanism used in the device deployment. Other major considerations include avoiding interference with recreational and fishing vessels, examining sensitive biological resources and species that could possibly be affected in the surrounding areas, and methods for transporting the extracted energy to shore. These are all important research topics along with the development and realization of more efficient and non-intrusive tidal power conversion devices.

REFERENCES

Blanchfield, J., Garrett, C., Rowe, A., Wild, P. (2008). "Tidal stream power resource assessment for Masset Sound, Haida Gwaii". Proceedings of the Institution of Mechanical Engineers Part A: Journal of Power and Energy. 222, 485-492.

Blunden, L. S., and Bahaj, A. S. (2006). "Initial evaluation of tidal stream energy resources at Portland Bill, UK". Renewable Energy. 31, 121-132.

Blunden, L. S., and Bahaj, A. S. (2006). "Tidal energy resource assessment for tidal stream generators". Proceedings of the Institution of Mechanical Engineers Part A: Journal of Power and Energy. 221, 137-146.

Bryden, I. G., and Couch, S. J. (2006). "ME1 - marine energy extraction: tidal resource analysis". Renewable Energy. 31(2), 133-139.

Bryden, I. G., Couch, S. J., Owen, A., Melville, G. (2006). "Tidal current resource assessment". Proceedings of the Institution of Mechanical Engineers Part A: Journal of Power and Energy. 221, 125-135.

Bryden, I. G., Grinstead, T., Melville, G. T. (2004). "Assessing the potential of a simple tidal channel to deliver useful energy". Applied Ocean Research. 26, 198-204.

Bryden, I., and Melville, G. (2004). "Choosing and evaluating sites for tidal current development". Proceedings of the Institution of Mechanical Engineers, Part A: Journal of Power and Energy. 218(8), 567-577.

Couch, S. J., and Bryden, I. G. (2006). "Tidal current energy extraction: hydrodynamic resource characteristics". Proceedings of the Institution of Mechanical Engineers, Part M: Journal of Engineering for the Maritime Environment. 220(4), 185-194.

Couch, S. J., and Bryden, I. G. (2007). "Large-scale physical response of the tidal system to energy extraction and its significance for informing environmental and ecological impact assessment". OCEANS 2007 – Europe, 1-5.

Charlier, R. H. (2003). "A 'sleeper' awakes: tidal current power". Renewable and Sustainable Energy Reviews. 7, 515-529.

Chen, C., Beardsley, R. C., Cowles, G. (2006). **"**An unstructured grid, finite-volume coastal ocean model (FVCOM) system". Oceanography. 19(1), 78–89.

CU. DIVAST. Hydro-environmental Research Centre, Cardiff University, <http://www.cardiff.ac.uk/engin/research/sustainabilityenergy/hydro/index.html> (Accessed 2010).

Dacre, S. L., Bullen, C. (2001). "Pentland Firth tidal current energy feasibility study—Phase 1". RGU, Aberdeen and ICIT. Orkney, Edinburgh: Scottish Enterprise.

Defne, Z., Haas, K. A., Fritz, H. M., Cambazoglu, M. K. (2008). "Assessment of Tidal Currents along the Atlantic Coast of the Southeast USA for Energy Conversion: Case Study for Georgia". 2nd International Conference on Ocean Energy. October 15-17. Brest, France.

Defne, Z., Haas, K. A., Fritz, H. M. (2010). "Numerical Modeling of Tidal Currents and the Effects of Power Extraction on Estuarine Hydrodynamics Along the Georgia Coast, USA".

Denham, C. R. SeaGrid Orthogonal Grid Maker for Matlab. <http://woodshole.er.usgs.gov/staffpages/cdenham/public_html/seagrid/seagrid.html> (Accessed 2008).

DHI. MIKE21. DHI, <http://www.dhigroup.com/Software/Marine/MIKE21.aspx> (Accessed 2010).

Durran, Dale R. (1999). "Numerical methods for wave equations in geophysical fluid dynamics". New York etc, Springer.

Egbert, G., Bennett, A., Foreman, M. (1994). "TOPEX/Poseidon tides estimated using a global inverse model". Journal of Geophysical Research. 99(C12), 24821-24852.

Garrett, C. and Cummins, P. (2004). "Generating power from tidal currents". Journal of Waterway, Port, Coastal and Ocean Engineering. 130, 114–118.

Garrett, C. and Cummins, P. (2005). "The power potential of tidal currents in channels". Proceedings of the Royal Society A 2005. 461 (2060), 2563-2572.

Gill, A. B. and Kimber, J. (2005). "The potential for cooperative management of elasmobranchs and offshore renewable energy developments in UK waters". Journal of the Marine Biological Association of the United Kingdom. 85, 1075-1081.

Hagerman, G, Polagye, B, Bedard, R, and Previsic, M. (2006c). "Methodology for Estimating Tidal Current Energy Resources and Power Production by Tidal In-Stream Energy Conversion (TISEC) Devices". EPRI-TP-001 NA Rev 3. Electric Power Research Institute.

Haidvogel, D. B., Arango, H.G., Budgell, W. P., Cornuelle, B. D., Curchitser, E., Di Lorenzo, E., Fennel, K., Geyer, W. R., Hermann, A. J., Lanerolle, L., Levin, J., McWilliams, J. C., Miller, A. J., Moore, A. M., Powell, T. M., Shchepetkin, A. F., Sherwood, C. R., Signell, R. P., Warner, J., Wilkin, J. (2008). "Regional Ocean Forecasting in Terrain-following Coordinates: Model Formulation and Skill Assessment". Journal of Computational Physics. 227(7), 3595-3624.

Karsten, R. H., McMillan, J. M., Lickley, M. J., Haynes, R. D. (2008). "Assessment of tidal current energy in the Minas Passage, Bay of Fundy". Proceedings of the Institution of Mechanical Engineers. Part A: Journal of Power and Energy. 222, 493-507.

Khan, M. J., Iqbal, M. T., Quaicoe, J. E. (2008). "River current energy conversion systems: Progress, prospects, and challenges". Renewable and Sustainable Energy Reviews. 12, 2177-2193.

Lim, Y. S., Koh, S. L. (2010). "Analytical assessment on the potential of harnessing tidal currents for electricity generation in Malaysia". Renewable Energy. 35, 1024-1032.

Mellor, G. L. (2003). "Users guide for a three-dimensional, primitive equation, numerical ocean model (June 2003 version)". Princeton, NJ: Princeton University. 6-28.

Mukai, A. Y., Westerink, J. J., Luettich, R. A. and Mark, D. (2002). "Eastcoast 2001, A Tidal Constituent Database for Western North Atlantic, Gulf of Mexico, and Caribbean Sea". ERDC/CHL TR-02-24.

NGDC. Coast Line Extractor. < http://rimmer.ngdc.noaa.gov/coast/ > (Accessed 2008).

NOAA. Tides and Currents, Tidal Datums. <http://tidesandcurrents.noaa.gov/datum_options.html> (Accessed 2008).

NOS. Office of Coast Survey US Bathymetric & Fishing Maps, <http://map.ngdc.noaa.gov/website/mgg/fishmap/> (Accessed 2008)

Pawlowicz, R., Beardsley B., and Lentz S. (2002). "Classical tidal harmonic analysis including error estimates in MATLAB using T_TIDE". Computers and Geosciences. 28, 929-937.

Pearce, N. (2005). "Worldwide tidal current energy developments and opportunities for Canada's Pacific coast". International Journal of Green Energy. 2(4), 365-386.

Polagye, B., Malte, P., Kawasel, M., and Durran, D. (2008). "Effect of large-scale kinetic power extraction on time-dependent estuaries". Proceedings of the Institution of Mechanical Engineers Part A: Journal of Power and Energy. 222(A5), 471-484.

Robertson, R. (2006). "Modeling internal tides over Fieberling Guyot: resolution, parameterization, performance". Ocean Dynamics. 56(5-6), 430-444.

Rourke, F. O., Boyle, F., Reynolds, A. (2010). "Tidal energy update 2009". Applied Energy. 87, 398-409.

Scott, B. E. (2007). "A renewable engineer's essential guide to marine ecology". Institute of Electrical and Electronics Engineers Computer Society, Piscataway, NJ 08855-1331, United States, Aberdeen, Scotland, United Kingdom, 4302218.

Shchepetkin, A. F. and McWilliams, J. C. (2005). "The Regional Ocean Modeling System (ROMS): A split-explicit, free-surface, topography-following coordinates ocean model". Ocean Modeling. 9, 347-404.

Shields, M. A., Dillon, L. J., Woolf, D. K., Ford, A. T. (2009). "Strategic priorities for assessing ecological impacts of marine renewable energy devices in the Pentland Firth (Scotland, UK)". Marine Policy. 33, 635-642.

Sutherland, G., Foreman, M., Garrett, C. (2006). "Tidal current energy assessment for Johnstone Strait, Vancouver Island". Proceedings of the Institution of Mechanical Engineers Part A: Journal of Power and Energy. 221, 147-157.

Teledyne RD Instruments (2008). “Workhorse Monitor: Direct-Reading 1200, 600, 300 kHz ADCP”. Poway, CA.

TELEMAC. TELEMAC System. <http://www.telemacsystem.com > (Accessed 2010).

Triton Consultants Ltd. (2002). Green Energy Study for British Columbia. Phase 2: Mainland.Tidal Current Energy. Chapter 6: Technology Review. Prepared for BC Hydro, Engineering.

U.S. Energy Information Administration. Independent Statistics and Analysis. <http://www.eia.doe.gov/emeu/recs/contents.html> (Accessed 2010).